

Syntheses, Structures, and Comparison of the Photophysical Properties of Cyclometalated Iridium Complexes Containing the Isomeric 1- and 2-(2'-pyridyl)pyrene Ligands

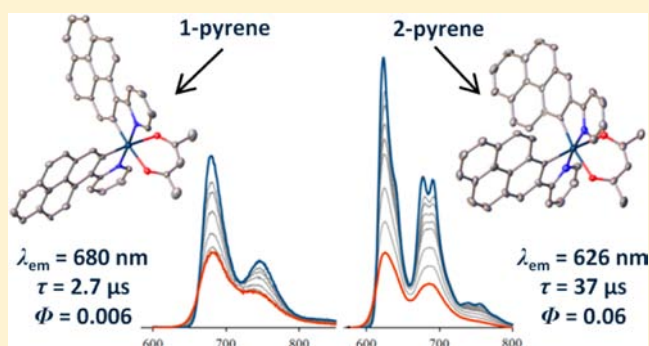
Robert M. Edkins,^{†,§} Katharina Fucke,^{†,§} Michael J. G. Peach,^{†,‡} Andrew G. Crawford,[†] Todd B. Marder,^{†,§} and Andrew Beeby^{*,†}

[†]Department of Chemistry, Durham University, South Road, Durham DH1 3LE, United Kingdom

[‡]Department of Chemistry, Faraday Building, Lancaster University, Lancaster LA1 4YB, United Kingdom

Supporting Information

ABSTRACT: Two cyclometalated iridium complexes of the form $\text{IrL}_2(\text{acac})$ have been synthesized, where L is either of the isomeric ligands 1- or 2-(2'-pyridyl)pyrene (1-ppyrH or 2-ppyrH). These complexes have been investigated in terms of their photophysical behavior and, although both complexes exhibit similar pure radiative lifetimes, they have substantially different observed phosphorescence lifetimes and quantum yields. Moreover, the observed phosphorescence lifetimes and quantum yields of both complexes, as well as the absorption spectra of $\text{Ir}(1\text{-ppyr})_2(\text{acac})$, exhibit a strong solvent dependence, while there is essentially no solvatochromism in the emission spectra of either complex. Single-crystal X-ray diffraction studies of both ligands and both iridium complexes reveal structural differences between the two isomers. The crystal structures of the ligands, supported by density functional theory (DFT) modeling, show that a twist is present between the pyridyl and pyrenyl rings in 1-ppyrH, but is absent in 2-ppyrH, which leads to the requirement for more unusual cyclometalation conditions for 1-ppyrH. Furthermore, it is suggested that the strained structure of $\text{Ir}(1\text{-ppyr})_2(\text{acac})$ provides access to a facile nonradiative excited state deactivation pathway, which leads to the higher value of k_{nr} for this isomer. DFT, TD-DFT, and ΔSCF calculations have been conducted to investigate further the photophysical properties of the complexes, allowing a detailed comparison of the two isomers. We find that Tamm-Dancoff Approximation TD-DFT with the CAM-B3LYP functional provides the best agreement between experimentally and theoretically determined transition energies, performing better than the more common combination of TD-DFT with B3LYP, the reasons for which are outlined. We also highlight some difficulties with performing optimization calculations on oxidized complexes to assess electrochemical data.



INTRODUCTION

Cyclometalated iridium(III) complexes have become the focus of intense research, spurred by the commercialization of these compounds as components of organic light-emitting devices (OLEDs).^{1,2} In particular, their high photoluminescence quantum yields (PLQY, Φ),^{3,4} facile color tuning by ligand modification,^{5–9} and relatively short phosphorescence lifetimes (τ) ($\Phi = 0.9$ and $\tau = 1.6 \mu\text{s}$ for $\text{Ir}(\text{ppy})_3$ (where ppyH is 2-phenylpyridine) in degassed CH_2Cl_2 solution),¹⁰ make them appealing for display screen applications. These same properties make these materials attractive for use as biological imaging agents,¹¹ components of dye-sensitized solar cells (DSSC),¹² and photocatalytic water splitting systems;¹³ however, most often for these particular applications, charged complexes are required to facilitate water solubility. Although complexes have now been designed and synthesized with emission spectra that collectively span the complete visible spectrum, producing

species that emit efficiently at the extremes of this spectral range remains a challenge.¹⁴

Pyrene is a polycyclic aromatic hydrocarbon exhibiting interesting photophysical properties, such as a long fluorescence lifetime ($\tau = 410 \text{ ns}$ in ethanol),¹⁵ excimer emission,¹⁶ and a high PLQY ($\Phi = 0.65$ in cyclohexane),¹⁷ and its utilization for organic electronics has recently been extensively reviewed.¹⁸ The photophysical properties of pyrene derivatives are particularly sensitive to the position of substitution, attributed to differences in orbital overlap and, importantly, symmetry.¹⁹ It was therefore conceived that the introduction of cyclometalated pyrene into an iridium complex would produce species with interesting photophysical properties. In addition, we were interested in probing the influence of substitution

Received: April 3, 2013

Published: August 14, 2013

pattern in pyrene-based organometallic systems and its subsequent effect on the observed photophysical behavior.

Most studies of the incorporation of pyrene into metal complexes have focused on attaching the pyrene as a pendant to a common ligand, for example, onto an iridium complex with a terpyridine ligand,²⁰ a Pt acetylide,²¹ or several Ru bipyridine²² and terpyridine²³ complexes. Other recent examples include a neutral cyclometalated iridium complex in which energy transfer to a pyrene-conjugated acetylacetonato (acac) ancillary ligand was investigated in detail²⁴ and an ionic iridium complex with energy transfer to a pyrene-substituted bipyridyl ligand.²⁵ The majority of these studies mentioned have centered on 1-pyrenyl derivatives due to the ease of their synthesis. There have only been a few studies of organometallic pyrene complexes and the effect of metal coordination directly onto pyrene, which have included examples of σ -bonded Au(I),^{26,27} Ru(II),²⁸ and Pd(II) and Pt(II)²⁹ complexes. Ionkin and co-workers³⁰ have shown that 1-(2'-pyridyl)pyrene (1-pyprH) can be cyclometalated with Ir(III) at the 2-position of the pyrene ring; however, no photophysical properties of these materials were reported. More recently, this ligand has been used to prepare a cyclometalated Pt(II) complex, which was shown to be a weakly red-emitting species ($\lambda_{em} = 680$ nm, $\Phi = 0.005$ in degassed CH_2Cl_2 solution) with a multicomponent emission profile.³¹ In addition, an isoquinoline analogue of 1-pyprH (i.e., 1-(1'-isoquinolinyl)pyrene) has been reported as a cyclometalating ligand for Ir(III), although emission was not observed in solution.³² The isomeric 2-(2'-pyridyl)pyrene (2-pyprH) ligand has not been reported previously. In this paper, we show that making this subtle change to the ligand structure can result in profound differences in the photophysical, electronic, and structural properties of the resultant cyclometalated complexes of the form $\text{IrL}_2(\text{acac})$ (where L represents either 1- or 2-pypr).

EXPERIMENTAL METHODS

General Procedures. Where required, anhydrous and anaerobic conditions were maintained via standard Schlenk techniques, using solvents dried by a solvent purification system (Innovative Technologies) and operating under an inert atmosphere of dry nitrogen. Deionized water was used. All reagents were purchased from Sigma-Aldrich, Acros, Alfa Aesar, Fisher Scientific, or Precious Metals Online and used as received, without further purification. The compounds 1-bromopyrene,³³ 2-bromopyrene,³⁴ prepared from 2-(Bpin)pyrene,^{34–36} and 2-(tri-*n*-butylstannyl)pyridine³⁷ were synthesized as previously reported. Column chromatography was performed on silica gel and monitored via thin layer chromatography (TLC), using 254 nm fluorescent silica plates (Polygram Sil G/UV254 0.2 mm silica) visualized under UV light or by I_2 staining. All enantiomeric iridium complexes were isolated as racemic mixtures. Care was taken to minimize the exposure of the complexes to light while in chlorinated solvents during preparative, purification, and analytical stages, because it had been observed previously in both luminescence and NMR spectroscopy experiments that related complexes can be photolytically degraded in these solvents. NMR spectra were recorded on Varian Mercury-400, Varian VNMRS-600 or Varian VNMRS-700 spectrometers. J -coupling (^1H – ^1H) values are given in units of hertz (Hz) and chemical shifts (δ) are given in units of parts per million (ppm); these values were internally referenced to residual protiated solvent or the solvent ^{13}C resonance. Mass spectrometry (MS) was performed using a Waters Xevo QTOF equipped with an Atmospheric Solids Analysis Probe (ASAP) or via gas-chromatography coupled with mass spectrometry (GC-MS) with electron impact (EI) ionization. GC-MS was performed using an Agilent Technologies Model 6890 N chromatograph equipped with a Model 5983 inert mass-selective detector and a 10 m fused-silica capillary column (5% cross-linked

phenylmethylsilicone) using ultrahigh-purity helium as the carrier gas with the following conditions: injector temperature, 250 °C; detector temperature, 300 °C; and the oven temperature was ramped from 70 °C to 280 °C at a rate of 20 °C min^{-1} . A CE-400 Elemental Analyzer was used for elemental analysis (C, H, N). The melting points of the ligands were obtained by differential scanning calorimetry (DSC) (Model Q1000 DSC, TA Instruments) at a heating rate of 10 K min^{-1} . All samples were checked for purity by analytical TLC.

Photophysical Measurements. All photophysical measurements were made in solution using GPR-grade solvents. Ultraviolet–visible (UV-vis) absorption spectra of solutions in quartz cuvettes of path length $l = 1$ cm with an absorbance (A) of <0.3 at 400 nm were measured on a Unicam Model UV2-100 spectrometer operated with the Unicam Vision software. Baseline correction was achieved by reference to pure solvent in the same cuvette. Excitation and emission photoluminescence spectra were recorded on a Horiba Jobin–Yvon Model SPEX Fluorolog 3-22 spectrofluorometer. Samples were held in quartz fluorescence cuvettes with a 1 cm \times 1 cm square cross-section, degassed by repeated freeze–pump–thaw cycles until the pressure remained constant upon a new pump phase (typically 1.0×10^{-4} mbar) and sealed by a Teflon Young's tap. Solutions for emission spectroscopy had $A = 0.10$ – 0.15 at the excitation wavelength to minimize inner filter effects. PLQYs of the ligands and complexes were measured using the Fluorolog 3-22 and an integrating sphere using a published method.³⁸ DataMax software was used throughout. The photoluminescence lifetimes of the complexes were determined by a time-correlated multiphoton counting (TCMPC) method. In a homemade setup, the fundamental of an N_2 laser (337 nm, 10 μJ , 10 Hz) was used as an excitation source with emission detected in a 90° geometry by a Model ID-Quantique ID-100-50 single-photon counting avalanche diode at a wavelength selected by a monochromator with a 1 nm bandpass. The signal was digitized by a National Instruments (NI) USB-5133 (8 bit, 100 Ms s^{-1}) digitizer and processed and recorded by in-house LabVIEW (NI) software. Analysis was performed using Microsoft Excel. Variable-temperature emission spectra and lifetime measurements (77–298 K) were recorded using the same equipment detailed above, with the sample held in a liquid- N_2 -cooled Model DN 1704 Optical Cryostat (Oxford Instruments). The solvent mixture 5:5:2 diethyl ether:2-methylbutane:ethanol (EPA), which forms an optically transparent glass upon cooling ($T_g \approx 138$ K), was used for low-temperature measurements.

The fluorescence lifetimes were measured by time-correlated single photon counting (TCSPC), using 300 nm excitation. The excitation source used was the third harmonic of a mode-locked (900 nm), cavity-dumped (APE Pulse switch) Ti:sapphire laser (Coherent MIRA), pumped by the second harmonic (532 nm) of a continuous wave Nd:YAG laser (Coherent Verdi V6). The pulse characteristics were as follows: a temporal full width at half-maximum (fwhm) of ~ 150 fs, and an average power of 0.5 mW at a repetition rate of 4 MHz. The fluorescence emission was collected at right angles to the excitation source, with the emission wavelength selected using a monochromator (Jobin–Yvon TRIAX 190) and detected by a cooled photomultiplier tube module (IBH TBX-04). The instrument response function (IRF) was measured using a dilute LUDOX suspension as the scattering sample, giving an IRF of ~ 200 ps fwhm. Iterative deconvolution of the IRF with a decay function and nonlinear least-squares analysis were used to analyze the data.

Electrochemistry. Cyclic voltammetry was performed using dry CH_2Cl_2 as the solvent under an N_2 atmosphere in which the solution was maintained stationary. A scan rate (ν) of 100 mV s^{-1} was used with a 0.1 M [*n*-Bu₄N]PF₆ electrolyte solution at a concentration of ca. 1×10^{-4} M analyte. A gas-tight, single compartment, three-electrode cell equipped with a platinum disk working electrode, platinum wire counter electrode, and platinum wire pseudo-reference electrode was used and data collected on an Autolab PG-STAT 30 potentiostat. The working electrode was polished with alumina paste before each scan. Redox potentials have been adjusted such that they are reported relative to the ferrocene/ferrocenium (Fc/Fc⁺) couple at 0.0 V using an internal standard of the decamethylferrocene/decamethylferrocenium couple (Fc*/Fc**+) (Fc*/Fc**+ = -0.59 V vs. Fc/Fc⁺).³⁹

Computational Methods. Calculations were carried out using either the Gaussian 09 package⁴⁰ or, where stated, Q-Chem (version 4).⁴¹ Density functional theory (DFT) calculations were used to optimize the structures of the two complexes (lowest singlet (S_0) and triplet (T_1) states of the neutral species and the monocations (D_0) and dications (S_0)), using Becke's⁴² three-parameter hybrid exchange functional and the Lee–Yang–Parr⁴³ gradient-corrected correlation functional (B3LYP) with a mixed basis set of 6-31G(d)⁴⁴ for light atoms (H, C, N, O) and the Los Alamos National Laboratories second double- ζ (LANL2DZ)⁴⁵ basis set for both the valence and effective core potential functions of heavy atoms (Ir). Frequency calculations, performed on each optimized structure at the same level of theory, returned only positive (real) vibrational frequencies. Stability calculations, using the keyword *stable*, were performed for the first six eigenvectors (default). The stability calculations of the complexes at the S_0 optimized geometry indicated near instabilities ($\omega_{\text{STAB}} < 2$ eV) in the B3LYP wave function and true instabilities in the Hartree–Fock wave function ($\omega_{\text{STAB}} < 0$ eV) (see main text for a discussion of the implications of this result).^{46,47} Single-point energy calculations of the T_1 state at the optimized S_0 geometry ($T_1(S_0)$) and the S_0 state at the optimized T_1 geometry ($S_0(T_1)$) were performed for both complexes. These were used to obtain the dipole moment at these specific points and to calculate the self-consistent field energy difference (ΔSCF) between S_0 and $T_1(S_0)$ and between T_1 and $S_0(T_1)$. Time-dependent (TD)-DFT calculations were performed at the optimized S_0 (for absorption) and T_1 (for emission) geometries from the S_0 state to the lowest 20 states (1:1 singlet:triplet), using the same combination of B3LYP functional and 6-31G(d)/LANL2DZ mixed basis set. TD-DFT calculations using the Coulomb-attenuating method–B3LYP (CAM-B3LYP)⁴⁸ functional and Tamm–Dancoff Approximation^{49,50} TD-DFT⁵¹ calculations with both B3LYP and CAM-B3LYP functionals, all using the 6-31G(d)/LANL2DZ mixed basis set, were performed in Q-Chem for the lowest eight triplet states. Where stated, solvent was included in the calculations with the Polarizable Continuum Model (PCM) within Gaussian 09, modified to use the United-Atom Kohn–Sham (UAKS) Topological Model radii, which are optimized for use with a similar level of theory (PBE1PBE/6-31G(d)). Acetonitrile ($\epsilon_r = 35.688$) was chosen as the solvent, because it is the most polar solvent used experimentally and thus acts as the limiting case to compare with the gas-phase calculations. Potential energy surfaces of the ligands 1- and 2-pyrrH, as a function of the dihedral angle between the pyridine and pyrene rings, were calculated starting from the DFT optimized ground state geometry (B3LYP/6-31+G(d) level) by scanning this dihedral angle in fixed steps of 5° and optimizing all other degrees of freedom. TD-DFT calculations of both ligands were performed using the same 6-31+G(d) basis set with the B3LYP and CAM-B3LYP functionals. Orbital surfaces generated from the DFT calculations were viewed in the program GaussView 4.1. The initial geometry inputs for optimization calculations were based on the crystallographic coordinates in all cases and optimizations were carried out without any constraints.

Single-Crystal X-ray Diffraction. Single crystals were grown as follows: 1-(2'-pyridyl)pyrene (1-pyrrH) as colorless plates by evaporation of a CH_2Cl_2 solution of 1-pyrrH; 2-(2'-pyridyl)pyrene (2-pyrrH) as colorless prisms by evaporation of an acetonitrile solution of 2-pyrrH; $\text{Ir}(1\text{-pyrr})_2(\text{acac}) \text{CH}_2\text{Cl}_2$ monosolvate as orange blocks upon cooling a hot CH_2Cl_2 solution of $\text{Ir}(1\text{-pyrr})_2(\text{acac})$; $\text{Ir}(2\text{-pyrr})_2(\text{acac})$ as small orange needles by evaporation of a toluene solution of $\text{Ir}(2\text{-pyrr})_2(\text{acac})$.

Crystals suitable for single-crystal X-ray diffraction (XRD) structure determination were selected, soaked in perfluoropolyether oil, and mounted on MiTeGen sample holders. Crystallographic measurements of both Ir complexes and the 1-pyrrH ligand were carried out at 120 K using a Bruker SMART CCD 6000 single-crystal diffractometer equipped with an open flow N_2 Cryostream⁵² (Oxford Cryosystems) device, using graphite monochromated Mo $K\alpha$ radiation ($\lambda = 0.71073$ Å). Data for the 2-pyrrH ligand were collected at the same temperature on an Oxford Diffraction Gemini S Ultra diffractometer using graphite monochromated Mo $K\alpha$ radiation ($\lambda = 0.71073$ Å). For data reduction, the SAINT suite and the Oxford

Diffraction CrysAlis software version 1.171.33.55 were used; the structures were solved and refined with OLEX2.⁵³ All non-hydrogen atoms were treated anisotropically. Hydrogen atoms were calculated using riding models and refined isotropically.

Crystal Data for 1-pyrrH. $\text{C}_{21}\text{H}_{13}\text{N}$, 0.30 mm \times 0.14 mm \times 0.10 mm, $\rho = 1.397$ g cm^{-3} , monoclinic, $P2_1/c$, $Z = 4$, $a = 3.8499(5)$ Å, $b = 12.6863(15)$ Å, $c = 27.185(3)$ Å, $\beta = 90.715(5)^\circ$, $V = 1327.6(3)$ Å³, temperature 120(2) K, $\mu = 0.081$ mm⁻¹, 12745 measured reflections (3881 of which are independent), 1847 reflections with $I > 2\sigma(I)$, final R indices: $R_1 = 0.0630$ ($I > 2\sigma(I)$), $wR_2 = 0.1398$ (all data).

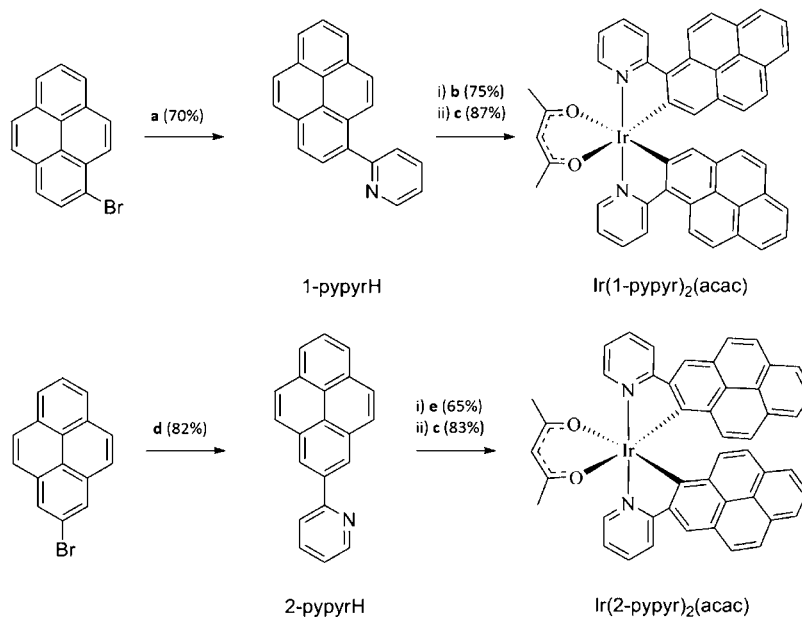
Crystal Data for 2-pyrrH. $\text{C}_{21}\text{H}_{13}\text{N}$, 0.25 mm \times 0.06 mm \times 0.05 mm, $\rho = 1.383$ g cm^{-3} , monoclinic, $P2_1/c$, $Z = 4$, $a = 4.5551(4)$ Å, $b = 22.119(2)$ Å, $c = 13.390(2)$ Å, $\beta = 96.148(12)^\circ$, $V = 1341.3(3)$ Å³, temperature 120(2) K, $\mu = 0.080$ mm⁻¹, 9403 measured reflections (2637 of which are independent), 1628 reflections with $I > 2\sigma(I)$, final R indices: $R_1 = 0.044$ ($I > 2\sigma(I)$), $wR_2 = 0.0873$ (all data).

Crystal Data for $\text{Ir}(1\text{-pyrr})_2(\text{acac})$. $\text{IrC}_{47}\text{H}_{31}\text{N}_2\text{O}_2\cdot\text{CH}_2\text{Cl}_2$, 0.08 mm \times 0.08 mm \times 0.02 mm, $\rho = 1.712$ g cm^{-3} , orthorhombic, $Pbcn$, $Z = 4$, $a = 7.8382(3)$ Å, $b = 22.5797(8)$ Å, $c = 20.4029(7)$ Å, $V = 3611.0(2)$ Å³, temperature 120(2) K, $\mu = 3.892$ mm⁻¹, 16 957 measured reflections (2603 of which are independent), 1702 reflections with $I > 2\sigma(I)$, final R indices: $R_1 = 0.0386$ ($I > 2\sigma(I)$), $wR_2 = 0.1040$ (all data).

Crystal Data for $\text{Ir}(2\text{-pyrr})_2(\text{acac})$. $\text{IrC}_{47}\text{H}_{31}\text{N}_2\text{O}_2$, 0.08 mm \times 0.05 mm \times 0.02 mm, $\rho = 1.668$ g cm^{-3} , monoclinic, $C2/c$, $Z = 8$, $a = 42.795(2)$ Å, $b = 8.9971(4)$ Å, $c = 18.0493(8)$ Å, $\beta = 103.618(1)^\circ$, $V = 6754.2(5)$ Å³, temperature 120(2) K, $\mu = 3.999$ mm⁻¹, 21900 measured reflections (4321 of which are independent), 2843 reflections with $I > 2\sigma(I)$, final R indices: $R_1 = 0.0395$ ($I > 2\sigma(I)$), $wR_2 = 0.0627$ (all data).

Synthesis. **Preparation of 1-(2'-pyridyl)pyrene (1-pyrrH).** The compounds 1-bromopyrene (283 mg, 1.0 mmol) and 2-(tri-*n*-butylstannyl)pyridine (90% purity, 0.40 mL, 450 mg, 1.2 mmol) were dissolved in toluene (7 mL) and degassed by three freeze–pump–thaw cycles. The catalyst $\text{Pd}(\text{PPh}_3)_2\text{Cl}_2$ (40 mg, 4 mol %) was added under nitrogen and the solution was heated to reflux at 110 °C for 20 h. After cooling to room temperature (r.t.), the solution was eluted through a plug of silica (CH_2Cl_2) and reduced in vacuo to give a yellow oil. A diethyl ether solution (10 mL) of the crude product was purified by extraction with aqueous HCl (5 M, 3 mL) and water (20 mL). The aqueous layer was neutralized with K_2CO_3 and subsequently re-extracted with CH_2Cl_2 (30 mL). The organic layer was dried over anhydrous K_2CO_3 , filtered, and concentrated in vacuo to give a cream white solid (196 mg, 70%). Upon storage under air for several weeks, the product turns dark yellow brown. Flash chromatography (SiO_2 ; CH_2Cl_2) can be used to remove the small quantity of brown impurity and recover the product as a cream white solid. Melting point (Mp): 87 °C (from CH_2Cl_2). Anal. calcd for $\text{C}_{21}\text{H}_{13}\text{N}$: C, 90.29; H, 4.69; N, 5.01%. Found C, 90.11; H, 4.68; N, 5.09%. ¹H NMR (400 MHz; CDCl_3): δ 8.89 (1 H, m), 8.40 (1 H, d, $J = 5.3$), 8.27 (1 H, d, $J = 8.0$), 8.19 (3 H, m), 8.10 (3 H, m), 8.05 (1 H, t, $J = 8.0$), 7.89 (1 H, m), 7.75 (1 H, m), 7.39 (1 H, m). ¹³C{¹H} NMR (101 MHz; CDCl_3): δ 159.7, 150.0, 136.6, 135.9, 131.6, 131.1, 128.8, 128.3, 128.1, 127.8, 127.7, 126.3, 126.0, 125.3, 125.0, 122.2. HR-MS (ASAP⁺): m/z 279.1038 [$\text{M}]^+$, calcd for $\text{C}_{21}\text{H}_{13}\text{N}$: 279.1048 ($|\Delta m/z| = 3.6$ ppm).

Preparation of 2-(2'-pyridyl)pyrene (2-pyrrH). The compounds 2-bromopyrene (383 mg, 1.36 mmol) and 2-(tri-*n*-butylstannyl)pyridine (90% purity, 0.50 mL, 570 mg, 1.54 mmol) were dissolved in toluene (10 mL) and degassed by three freeze–pump–thaw cycles. The catalyst $\text{Pd}(\text{PPh}_3)_4$ (50 mg, 4 mol %) was added under nitrogen and the solution was heated to reflux at 110 °C for 20 h. The solution was eluted through a plug of silica (CH_2Cl_2) and reduced in vacuo to give a yellow oil. A diethyl ether solution (10 mL) of the crude product was purified by extraction with aqueous HCl (5 M, 3 mL) and water (20 mL). The aqueous layer was neutralized with K_2CO_3 and subsequently re-extracted with CH_2Cl_2 (30 mL). The organic layer was dried over anhydrous K_2CO_3 , filtered and concentrated in vacuo to give a tan–brown solid (325 mg, 82%). Flash chromatography (SiO_2 ; CH_2Cl_2) can be used to remove the small quantity of brown impurity, recovering the product as a cream white solid, which

Scheme 1. Syntheses of the Cyclometalated Iridium Complexes Ir(1-pyppy)₂(acac) and Ir(2-pyppy)₂(acac)^a

^a(a) 2-(Tri-*n*-butylstannyl)pyridine, Pd(PPh₃)₂Cl₂ (4 mol %), N₂, 110 °C, 20 h; (b) IrCl₃·3H₂O, trimethyl phosphate, 90 °C, 36 h; (c) Acetylacetonone, K₂CO₃, 1:1 ethanol:acetone, 60 °C, 4 h; (d) 2-(Tri-*n*-butylstannyl)pyridine, Pd(PPh₃)₄ (4 mol %), N₂, 110 °C, 20 h; (e) IrCl₃·3H₂O, 2:1 2-ethoxyethanol:H₂O, 110 °C, 6 h.

recolorizes upon storage under air over a period of weeks. Mp: 138 °C (from CH₂Cl₂). Anal. calcd for C₂₁H₁₃N: C, 90.29; H, 4.69; N, 5.01%. Found C, 90.01; H, 4.70; N, 5.13%. ¹H NMR (400 MHz; CDCl₃): δ 8.83 (1 H, d, *J* = 4.9), 8.80 (2 H, s), 8.14–8.20 (4 H, m), 8.09 (2 H, d, *J* = 8.8), 8.06 (1 H, d, *J* = 7.8), 8.0 (1 H, t, *J* = 7.8), 7.86 (1 H, td, *J* = 7.8 and 1.7), 7.29–7.34 (1 H, m). ¹³C{¹H} NMR (101 MHz; CDCl₃): δ 158.0, 150.1, 145.2, 137.3, 137.0, 131.8, 131.6, 128.0, 126.4, 125.4, 125.2, 124.8, 123.6, 122.6, 121.7. HR-MS (ASAP⁺): *m/z* 280.1126 [M+H]⁺, calcd for C₂₁H₁₄N 280.1126 ($|\Delta m/z|$ = 0.0 ppm).

Preparation of [Ir(1-pyppy)₂(μ-Cl)]₂. The compounds 1-pyppyH (57 mg, 0.20 mmol) and IrCl₃·3H₂O (35 mg, 0.10 mmol) were dissolved in trimethyl phosphate (4 mL) and heated at 90 °C for 36 h. The suspension was filtered and the orange solid was washed with ethanol and dried under high vacuum (58 mg, 75%). The compound is virtually insoluble, hindering purification and analysis.

Preparation of [Ir(2-pyppy)₂(μ-Cl)]₂. The compounds 2-pyppyH (217 mg, 0.78 mmol) and IrCl₃·3H₂O (138 mg, 0.39 mmol) were dissolved in 2:1 2-ethoxyethanol:water (9 mL) and heated at reflux (110 °C) for 6 h, cooled to r.t., and stirred for an additional 16 h. During this time, the initially dark green solution turned orange. Water (20 mL) was added and the solution was filtered. The orange solid was washed with ethanol (3 × 10 mL) and dried under high vacuum to give a dark orange solid (199 mg, 65%). The compound is virtually insoluble, hindering purification and analysis.

Preparation of Ir(1-pyppy)₂(acac). The compounds [Ir(1-pyppy)₂(μ-Cl)]₂ (58 mg, 0.037 mmol), acetylacetonone (0.05 mL, 0.5 mmol (excess)), and K₂CO₃ (50 mg) were suspended in a 1:1 mixture of ethanol:acetone (10 mL) and heated at 60 °C for 4 h. The solution volume was reduced in vacuo to give an orange oil. This oil was triturated with hexanes (5 mL), filtered, dissolved in CH₂Cl₂, and evaporated in vacuo to give a dark orange solid (27 mg, 87%). ¹H NMR (700 MHz; CDCl₃): δ 8.89 (2 H, d, *J* = 9.4), 8.76 (4 H, m), 8.08 (2 H, d, *J* = 9.4), 8.04 (2 H, d, *J* = 7.5), 7.97 (2 H, td, *J* = 7.9 and 1.3), 7.92 (2 H, d, *J* = 7.5), 7.79 (2 H, t, *J* = 7.5), 7.70 (2 H, d, *J* = 8.9), 7.41 (2 H, d, *J* = 8.9), 7.29 (2 H, m), 6.87 (2 H, s), 5.32 (1 H, s), 1.82 (6 H, s). ¹³C{¹H} NMR (151 MHz; CDCl₃): δ 185.1, 169.4, 149.3, 148.6, 139.3, 137.0, 131.4, 130.4, 130.2, 129.4, 128.8, 128.4, 128.0, 127.3, 125.8, 125.6, 125.1, 124.4, 123.7, 122.6, 122.4, 121.3, 100.8, 28.9. HR-MS (ASAP⁺): *m/z* 847.2026 [M+H]⁺, calcd for ¹⁹¹IrC₄₇H₃₂N₂O₂ 847.2070 ($|\Delta m/z|$ = 5.2 ppm). We were not able to obtain satisfactory

elementary analysis data (low %C) for this isomer, attributable to nonstoichiometric loss of CH₂Cl₂ from the crystal lattice. This is supported by the traces of residual CH₂Cl₂ (ca. 0.4 eq. by integration) observable in the ¹H NMR spectrum of a vacuum-dried sample (see Figure S5 in the Supporting Information (SI)) and the single-crystal X-ray structure, which is that of a CH₂Cl₂ monosolvate when freshly removed from the mother liquor. Anal. calcd for: IrC₄₇H₃₁N₂O₂: C, 66.57; H, 3.68; N, 3.30% and for IrC₄₇H₃₁N₂O₂·0.4CH₂Cl₂: C, 64.53; H, 3.64; N, 3.18%. Found: C, 64.79; H, 3.64; N, 3.15%.

Preparation of Ir(2-pyppy)₂(acac). The compounds [Ir(2-pyppy)₂(μ-Cl)]₂ (15 mg, 0.01 mmol), acetylacetonone (0.05 mL, 0.5 mmol (excess)), and K₂CO₃ (50 mg) were suspended in a 1:1 mixture of ethanol:acetone (10 mL) and heated to 60 °C for 4 h. The solution volume was reduced in vacuo to give an orange oil. This oil was triturated with hexanes (5 mL), filtered, dissolved in CH₂Cl₂, and evaporated in vacuo to give a dark orange solid (14 mg, 83%). Anal. calcd for: IrC₄₇H₃₁N₂O₂: C, 66.57; H, 3.68; N, 3.30%. Found C, 66.70; H, 3.67; N, 3.23%. ¹H NMR (400 MHz; CDCl₃): δ 8.64 (2 H, s), 8.44 (2 H, d, *J* = 8.0), 8.30 (2 H, d, *J* = 5.6), 8.01 (2 H, d, *J* = 9.0), 7.97 (2 H, td, *J* = 8.0 and 1.6), 7.83 (2 H, m), 7.79 (2 H, d, *J* = 9.0), 7.68 (2 H, s), 7.67 (2 H, d, *J* = 1.6), 7.14 (2 H, d, *J* = 9.0), 7.06 (2 H, td, *J* = 8.0 and 6.7), 6.74 (2 H, d, *J* = 9.0), 5.05 (1 H, s), 1.63 (6 H, s); ¹³C{¹H} NMR (176 MHz; CDCl₃): δ 185.0, 168.9, 150.6, 149.5, 144.9, 139.1, 137.6, 132.5, 132.3, 131.0, 128.2, 127.1, 125.8, 125.7, 125.3, 125.2, 125.0, 123.0 (two environments resolved by ¹H–¹³C HSQC), 121.1, 120.5, 119.7, 100.0, 28.6. HR-MS (ASAP⁺): *m/z* 847.2073 [M+H]⁺, calcd for ¹⁹¹IrC₄₇H₃₂N₂O₂ 847.2070 ($|\Delta m/z|$ = 0.3 ppm).

RESULTS AND DISCUSSION

Synthesis. Pyrene is most commonly functionalized at the 1-position, which is the site susceptible to electrophilic substitution. Traditionally, the synthesis of 2-substituted derivatives required the reduction of pyrene to 4,5,9,10-tetrahydropyrene, substitution, and reoxidation,⁵⁵ which is both laborious and low yielding. Recently, it has become possible to readily functionalize the 2-position through an Ir(I) catalyzed C–H borylation,^{34–36} with the steric demand of the catalyst restricting the substitution to the 2-position, allowing

the regioselective synthesis of both of the precursors 1- and 2-bromopyrene through published methods.^{33,34} The two isomeric ligands were synthesized by Stille coupling of the respective 1- or 2-bromopyrene with 2-(tri-*n*-butylstannyl)pyridine in toluene at reflux for 20 h using either Pd(PPh₃)₂Cl₂ or Pd(PPh₃)₄ as the catalyst. Previously, the 1-pyprH ligand had been synthesized using Suzuki–Miyaura coupling of 1-pyrenylboronic acid and 2-bromopyridine in 47% yield.³¹ The Stille coupling used here affords this ligand in an improved yield of 70% and the novel 2-pyprH in 82% yield. Cyclometalation of pyrene-containing ligands at the 2-position of the pyrene ring has been described as occurring with difficulty,²⁸ while it has been shown that 1-pyprH can be complexed to iridium when trimethyl phosphate is used as the solvent.³⁰ Ionkin has proposed that using this particular solvent increases the rate of cyclometalation for otherwise low-reactivity ligands by removing the hydrogen chloride generated in the reaction, as well as by improving the solubility of the reactants, and has shown it to be effective for a range of examples.^{30,56–58} Following this procedure, we obtained the diiridium μ -chloro-bridged dimer from 1-pyprH in a yield of 75% after heating at 90 °C for 36 h. A standard protocol for cyclometalation was used for the analogous dimer of the 2-pyprH ligand, using a 2:1 mixture of 2-ethoxyethanol and water as the solvent, with a shorter reaction time of 6 h at 110 °C, yielding the desired dimer in 65% yield. Surprisingly, the more sterically hindered 1-(1'-isoquinoliny)pyrene has been reported to cyclometalate in 3:1 2-ethoxyethanol:water mixture within 6–7 h.³² The absence of an X-ray structure for this complex, however, means that the possibility of this product being the less sterically demanding 6-membered chelate, cyclometalated at the 10-position, cannot be ruled out. Indeed, Pope and co-workers⁵⁹ very recently reported some related Ir(III) complexes with similarly bulky 1-(2'-benzimidazolyl)pyrene ligands that were found to be cyclometalated at the 10-position, including the X-ray structure of one derivative. The dimers proved to be highly insoluble in common solvents, making their full characterization difficult, as reported for [Ir(1-pyprH)₂(μ -Cl)]₂.³⁰ The crude dimers were reacted with acetylacetonate in the presence of K₂CO₃ as a base to afford the more-soluble IrL₂(acac) complexes in high yields (83–87%). The synthetic pathways are summarized in Scheme 1.

X-ray Crystallography. The molecular structures of the ligands 1-pyprH and 2-pyprH and the complexes Ir(1-pyprH)₂(acac) and Ir(2-pyprH)₂(acac) were determined by single-crystal X-ray diffraction. The structures of the two ligands are shown in Figure 1. Details of the crystallization procedures and the important crystallographic parameters can be found in the experimental section, while full CIFs are available in the SI.

Both ligands crystallize in the *P*2₁/*c* space group and both structures show disorder in the orientation of the pyridine rings, which was modeled across two sites at 50% occupancy each. This is likely to be due to the similarity in size of CH and N and the lack of intermolecular interactions, in particular, the absence of a hydrogen-bond donor group, which might be predicted to lead to a preference of one site over the other. In 1-pyprH, there is a 41° torsional twist between the planes of the pyridine and pyrene rings that is absent in 2-pyprH (torsion angle of 0°). Although this twist could be brought about by crystal packing forces, it is likely that it is a result of a steric interaction between the hydrogen in the 3-position of the pyridine and those at the 1- and/or 10-position of the pyrene

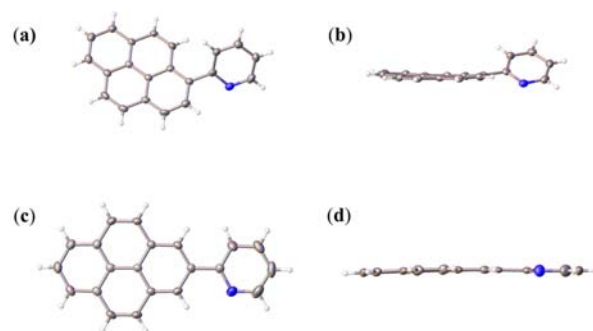


Figure 1. Molecular structures of the isomeric ligands 1-pyprH and 2-pyprH as obtained by single-crystal X-ray diffraction (XRD): (a) 1-pyprH front view, (b) 1-pyprH side view, (c) 2-pyprH front view, and (d) 2-pyprH side view. Atomic displacement parameters are illustrated as 50% probability surfaces. Element (color): carbon (gray), nitrogen (blue), hydrogen (white). In both structures, the pyridine rings are disordered over two sites and have been modeled with 50% occupancy of the two orientations. Only one orientation is shown here for clarity.

ring (vide infra). The crystal packing shows the expected π – π stacking, with pyrene–pyrene interplanar distances of 3.53 and 3.45 Å for 1- and 2-pyprH, respectively, where the slightly longer distance for 1-pyprH is attributable to its twisted conformation. See Figures S9 and S10 in the SI for crystal packing diagrams and description.

The structures of the two iridium complexes are shown in Figure 2. Both complexes have mutually *trans* pyridines, as is common in this class of complex, which is a fact also revealed by the single set of resonances for the magnetically equivalent cyclometalated ligands in both the ¹H and ¹³C{¹H} NMR spectra. The structure of Ir(1-pyprH)₂(acac) has a twist of 18° between the planes of the pyridine and pyrene rings, because of a steric interaction, analogous to that observed in the structure of the free ligand, which is again not present in Ir(2-pyprH)₂(acac) (dihedral angle of 0°). Therefore, complexation of the 1-pyprH ligand has reduced the torsional angle between the rings, compared to the free ligand, and thus increased the steric interaction between the hydrogen atoms at the 3-position of the pyridine ring and the 10-position of the pyrene. This increase in steric interaction, coupled with the greater reactivity of pyrene at the 1-position, may account for the more unusual conditions required to complex the 1-pyprH ligand,³⁰ compared to those employed for 2-pyprH. A similar explanation has been invoked for the difficulty of cyclometalating 1-(2'-quinoliny)pyrene with ruthenium.²⁸

Unlike the reported structures of the related heteroleptic complex with the ligand 1-(2'-(4'-methylpyridyl))pyrene and an anionic P[^]N chelating ancillary ligand,³⁰ the pyrene rings do not exhibit π – π stacking. Ir(1-pyprH)₂(acac) forms a CH₂Cl₂ monosolvate in which the solvent molecule fills voids in the structure rather than intercalating between layers of pyrene rings as was seen previously in both the CH₂Cl₂ and acetone solvates of the related compound (CSD Refcodes: OCOTOQ and ODELAL, respectively).

Photophysical Study. Ligands. The photophysical properties of the two ligands are presented in Figure 3 and are summarized in Table 1. In analogy with the parent compound pyrene and other substituted derivatives,¹⁹ the intense absorption bands at ca. 340 nm present for both compounds are assigned as the ¹L_a transitions (essentially LUMO ← HOMO). The 2-pyprH ligand shows pronounced vibrational

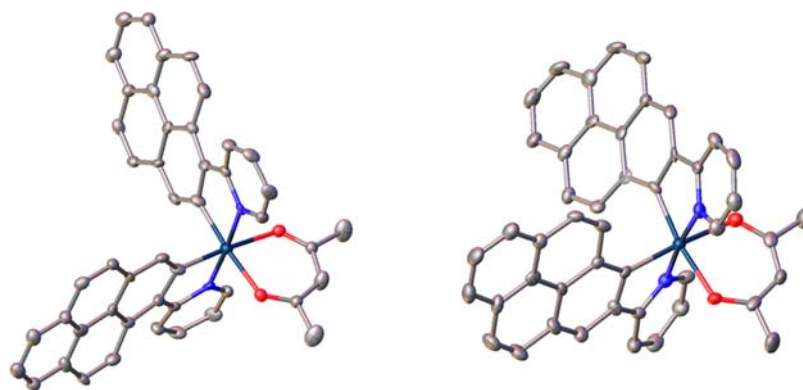


Figure 2. Molecular structures of Ir(1-pyppy)₂(acac) (left) and Ir(2-pyppy)₂(acac) (right) as obtained by single-crystal X-ray diffraction (XRD). Atomic displacement parameters are illustrated as 50% probability surfaces. Element (color): iridium (dark green), carbon (gray), oxygen (red), nitrogen (blue). The structure of Ir(1-pyppy)₂(acac) contains a disordered CH₂Cl₂ solvate molecule (not shown) that was modeled with 50% occupancy in two orientations. Hydrogen atoms have been omitted for clarity.

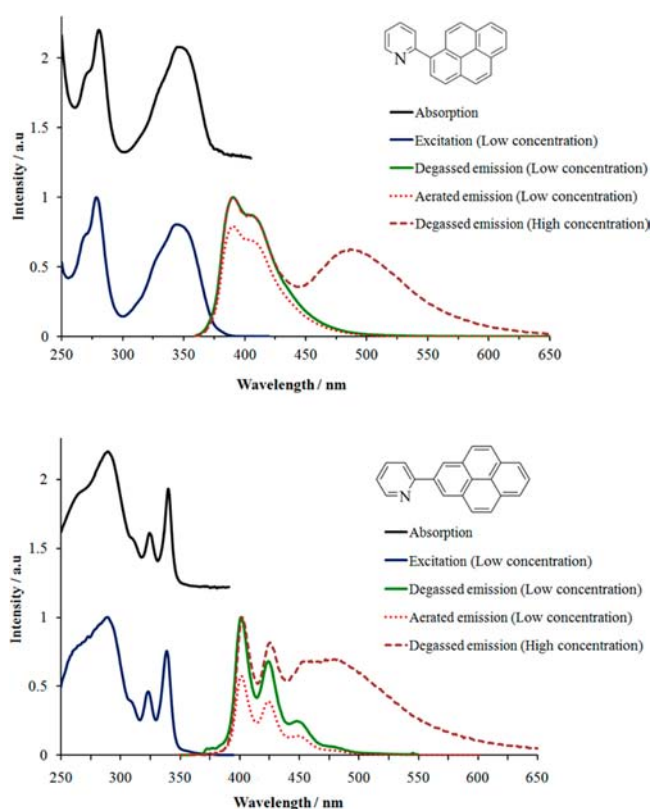


Figure 3. Room-temperature normalized absorption, excitation, and emission ($\lambda_{\text{ex}} = 340$ nm) spectra of 1-pyppyH (top) and 2-pyppyH (bottom) in CH₂Cl₂. Excitation spectra of 1- and 2-pyppyH were independent of λ_{em} ($\lambda_{\text{em}} = 425$ nm shown). Aerated emission spectra are normalized relative to the degassed emission spectra recorded under identical conditions. The absorption spectra have been offset for clarity. Low concentration and high concentration refer to concentrations of ca. 10^{-6} mol dm⁻³ and ca. 10^{-4} mol dm⁻³, respectively.

structure to this band with an energy spacing of 1470 cm^{-1} , while for 1-pyppyH this band is broad and structureless, with the exception of a poorly resolved high-energy shoulder. This can be attributed to a combination of two factors. The symmetry along the long axis where the 1L_a transition dipole moment lies in pyrene is maintained in 2-pyppyH, whereas in the 1-pyppyH compound, this symmetry is broken, leading to a

mixing of states. In the 1-pyppyH compound, there is better orbital overlap, allowing charge-transfer transitions to the pyridine from the pyrene that additionally broaden the band.³¹ Charge transfer is moderated in 2-pyppyH due to the nodal plane that lies along the long axis of pyrene and through the 2-position in both the HOMO and the LUMO (see Table S1 in the SI). Absorption bands are observed at ca. 290 nm for both compounds with differing intensity and spectral width. The weakly allowed 1L_b (mixed LUMO \leftarrow HOMO-1 and LUMO +1 \leftarrow HOMO) transitions are poorly resolved and are located at lower energy than the 1L_a band for 2-pyppyH and coincidental with this band for 1-pyppyH. Justification for this assignment can be found in the computational study section (vide infra).

The compound 2-pyppyH shows emission with well-resolved vibrational structure, whereas the 1-pyppyH ligand, in which the symmetry is broken and charge-transfer (CT) transitions are feasible, exhibits a broader profile. The emission is also oxygen sensitive as can be seen by the diminished intensity under aerated conditions, although the spectral profile is unaffected. The sensitivity of the 2-pyppyH ligand to oxygen is greater than that of 1-pyppyH, which can be attributed to the longer lifetime of the 2-substituted pyrene compound, as observed for other derivatives.¹⁹ Both ligands show excimer emission at high concentration (ca. 10^{-4} mol dm⁻³) with a band centered at 483 and 475 nm for 1-pyppyH and 2-pyppyH, respectively. This is similar to the excimer emission of pyrene, which is centered at 480 nm and is observed at concentrations above 10^{-5} mol dm⁻³.¹⁶

Complexes. Often the absorption spectra of cyclometalated iridium complexes are assigned as being composed of individual ligand centered (LC) and metal to ligand charge transfer (MLCT) bands with the MLCT placed at lower energy. This has often been based on theoretical and experimental studies of the parent complex Ir(ppy)₃ and related compounds.⁶⁰ However, the true nature of each transition for a new complex is often not fully elucidated and is likely an admixture of LC and MLCT, as well as intraligand charge transfer (ILCT) character. Furthermore, the singlet or triplet nature of these transitions may not be defined absolutely due to the large spin-orbit coupling induced by the Ir atom; however, this notwithstanding, here, we refer to bands as formally singlet or triplet, for the sake of simplicity. The absorption spectra of Ir(1-pyppy)₂(acac), in a range of solvents, are displayed in

Table 1. Photophysical Data for the Ligands 1-pyppyH and 2-pyppyH in Dichloromethane

compound	λ_{abs} (nm) ^a (log(ϵ (M ⁻¹ cm ⁻¹)))	λ_{em} (nm) ^{b,c}	$\Phi^{b,d}$		τ (ns) ^e
			aerated/degassed	aerated/degassed	
1-pyppyH	271 (4.08), 280 (4.25), 345 (4.18)	389*, 403, 483 (excimer)	0.43 ^f /0.55		9.8 ^g /12.9
2-pyppyH	264 (sh., 4.09), 288 (4.24), 308 (3.77), 323 (3.86), 339 (4.12), 385 (2.00)	401*, 423, 446, 476, 475 (excimer)	0.20/0.36		12.0/21.2

^ash. = shoulder. ^bExcitation at 340 nm. ^cPeaks assigned as excimer are observed only at high (ca. 10⁻⁴ mol dm⁻³) concentration. All other peaks are observed at high and low (ca. 10⁻⁶ mol dm⁻³) concentrations. Starred value is the emission maximum at low concentration. ^dEstimated error: 10% of the value. ^eExcitation at 300 nm. Decay monitored at 400 nm. Estimated error: 5% of the value. ^fReported previously as 0.41 (ref 31). ^gReported previously as 3 ns (ref 31).

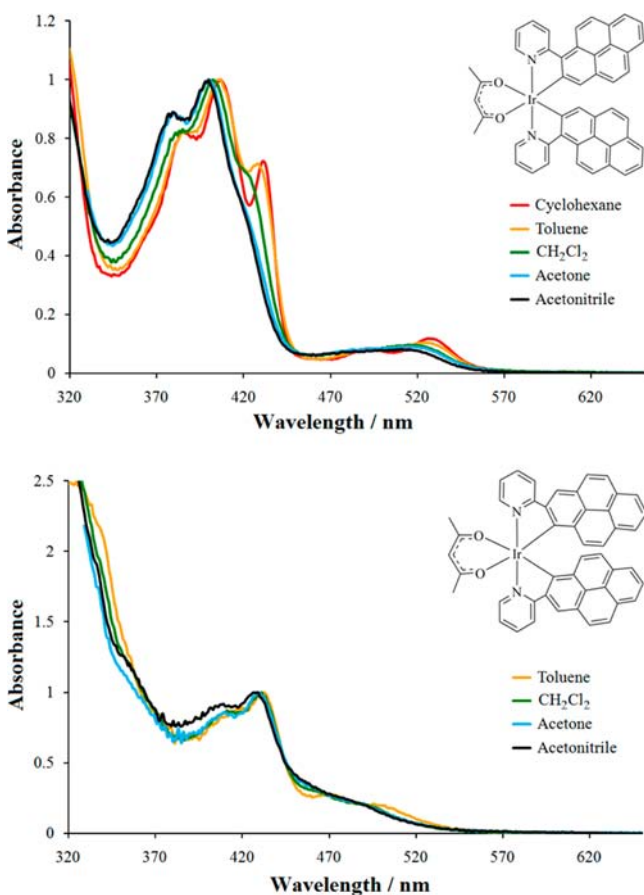


Figure 4. Absorption spectra of Ir(1-pyppy)₂(acac) (top) and Ir(2-pyppy)₂(acac) (bottom) in a range of solvents of different polarity. The spectra have been normalized to the bands centered at 400 and 430 nm, respectively. *N.B.* Because of low solubility, the absorption spectrum of Ir(2-pyppy)₂(acac) was not measured in cyclohexane.

Figure 4. In these spectra, there is an intense absorption band at higher energy than 350 nm, which would typically be assigned as the ¹LC transition, and this convention is followed here. The band centered at approximately 400 nm is structured, which would imply significant ¹LC character for this transition as well. Of particular note is the modest negative solvatochromic shift of this band that can be interpreted as a stabilization of the ground state in more polar solvents. Not only is there a blue-shift of the peak of this band by ~450 cm⁻¹ from cyclohexane to acetonitrile, but there is also a change in profile. In cyclohexane, there are three resolved vibronic bands with ~1240 cm⁻¹ spacing, the lowest energy of which is reduced in intensity in toluene, further reduced to a shoulder in CH₂Cl₂, and is completely absent in acetonitrile. Acetone and acetonitrile solutions produce almost identical features in this

region, and thus no further stabilization is achieved with solvents having a greater polarity than acetone. This broadening of the absorption band in more polar solvents is potentially an indication of the greater CT character (either ¹MLCT or ¹ILCT type) of the transition in these solvents. At lower energy, centered at 520 nm, is a second structured band that again broadens in profile with increasing solvent polarity and is also assigned as having mixed ³LC and generic ³CT character dependent on solvent environment, with its lower extinction coefficient an indication that it is likely a triplet transition partially facilitated by the Ir atom.

The Ir(2-pyppy)₂(acac) isomer exhibits an absorption profile that is much broader and less structured than the previously discussed isomer, because of the greater overlap of the various bands. However, it does still have bands that can be identified as ¹LC-type at wavelengths below 370 nm, a combination ¹LC and ¹CT band at ~430 nm and a less intense feature centered at 490 nm that is described as an admixture of ³LC and ³CT. The 430 nm centered band is bathochromically shifted by ~1700 cm⁻¹ compared to the 1-substituted isomer, while the lowest energy band does not extend as far toward the red end of the spectrum. In addition, this isomer does not show such a dramatic solvent dependence; the band shape is predominantly maintained and there is a smaller negative solvatochromic shift of 200 cm⁻¹ of the 430 nm centered band.

Comparing the room temperature emission spectra (Figure 5) of the two complexes in acetonitrile, there is an energy difference in the emission maxima of 1350 cm⁻¹ ($\lambda_{\text{em}} = 623$ nm for Ir(2-pyppy)₂(acac) and $\lambda_{\text{em}} = 680$ nm for Ir(1-pyppy)₂(acac)). In both cases, the emission spectra are almost solvent-independent (<100 cm⁻¹ negative solvatochromic shift

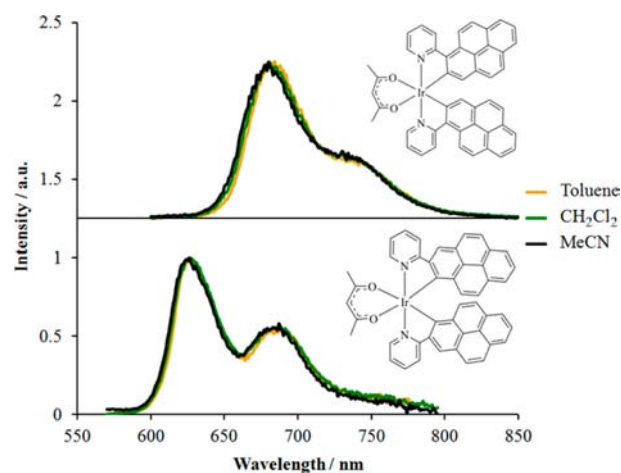


Figure 5. Normalized room-temperature emission spectra of Ir(1-pyppy)₂(acac) (top, $\lambda_{\text{ex}} = 400$ nm) and Ir(2-pyppy)₂(acac) (bottom, $\lambda_{\text{ex}} = 430$ nm) in a range of solvents of different polarity.

between toluene and acetonitrile), implying that the transition can be described as predominantly ^3LC . The assignment of a ^3LC -type transition is further supported by the structured emission for $\text{Ir}(\text{2-pyppy})_2(\text{acac})$ with a vibrational spacing of 1350 cm^{-1} . The emission spectrum of $\text{Ir}(\text{1-pyppy})_2(\text{acac})$ is similar in profile, but shows a less well-resolved vibronic band as a shoulder. This implies that this isomer has a more pronounced geometry change in the excited state, which can be attributed to electronic coupling between the pyridyl and pyrenyl moieties leading to a degree of $^3\text{ILCT}$. For comparison, the inclusion of either isomer of the pyrenyl unit in place of a phenyl ring leads to significantly bathochromically shifted emission relative to the parent complex $\text{Ir}(\text{ppy})_2(\text{acac})$, which has an emission maximum at 520 nm in CH_2Cl_2 ;⁶¹ this corresponds to a shift of 4500 cm^{-1} for $\text{Ir}(\text{1-pyppy})_2(\text{acac})$ and 3300 cm^{-1} for $\text{Ir}(\text{2-pyppy})_2(\text{acac})$. $\text{Ir}(\text{ppy})_2(\text{acac})$ is also much more solvatochromic due to the predominantly $^3\text{MLCT}$ nature of its emission.⁵⁴

Emission and excitation spectra for both complexes were additionally obtained at 77 K in the optically transparent, mixed-solvent glass EPA (5:5:2 diethyl ether:2-methylbutane:ethanol) and are shown in Figure 6. For both $\text{Ir}(\text{1-pyppy})_2(\text{acac})$ and $\text{Ir}(\text{2-pyppy})_2(\text{acac})$, the emission maximum

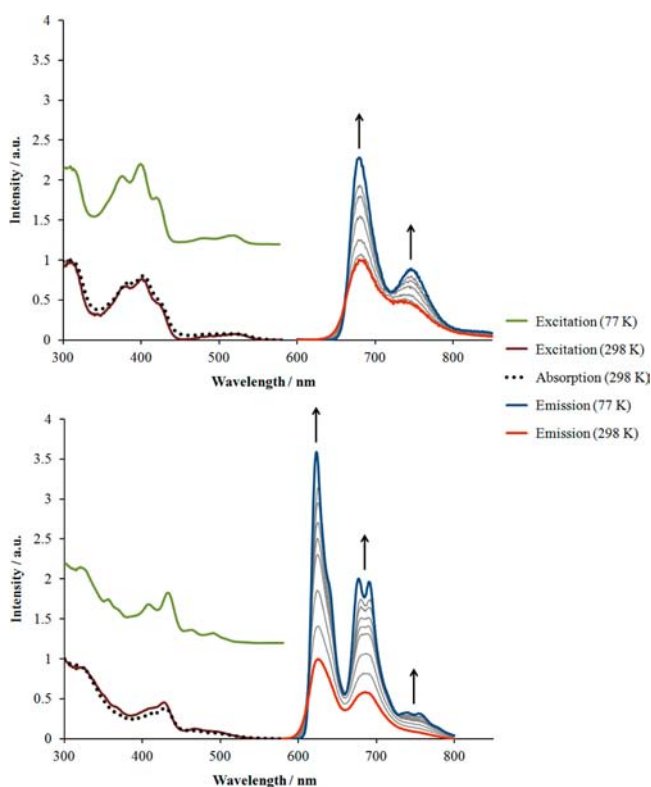


Figure 6. Normalized room-temperature absorption and variable-temperature excitation and emission spectra of $\text{Ir}(\text{1-pyppy})_2(\text{acac})$ (top, $\lambda_{\text{em}} = 680\text{ nm}$, $\lambda_{\text{ex}} = 400\text{ nm}$) and $\text{Ir}(\text{2-pyppy})_2(\text{acac})$ (bottom, $\lambda_{\text{em}} = 630\text{ nm}$, $\lambda_{\text{ex}} = 430\text{ nm}$) in the solvent mixture 5:5:2 diethyl ether:2-methylbutane:ethanol (EPA). Variable-temperature emission spectra are normalized relative to the 298 K spectrum and the spectra in gray were recorded at intervals during the cooling of the sample to 77 K . The excitation spectra at 77 K are offset for clarity. The arrows indicate the change in intensity with decreasing temperature (N.B. the volume contraction of EPA ($V_{77\text{ K}}/V_{298\text{ K}} = 0.77$)⁶² only partially accounts for the increase in intensity). Note that the absorption and excitation spectra at 298 K are in good agreement, as expected.

is temperature-independent, giving $T_1 - S_0 E_{0,0} = 14\,700\text{ cm}^{-1}$ and $16\,100\text{ cm}^{-1}$, respectively. The negligible temperature-induced shift of the emission lends further support for the assignment of a large ^3LC component to the transition. Other features of the low-temperature spectra include the expected sharpening of the high-energy edge of the emission band and an increase in the resolution of the vibronic structure. This is most notable for $\text{Ir}(\text{2-pyppy})_2(\text{acac})$ for which the second vibrational band at r.t. splits into two peaks of $\sim 350\text{ cm}^{-1}$ spacing at 77 K , potentially indicating a low-energy vibrational mode coupling the excited and ground states. Further structure to the low-energy tail of the emission spectrum becomes apparent, also with an energy spacing of ca. 350 cm^{-1} . Both compounds exhibit a moderate increase in intensity at 77 K , which was monitored during the cooling process. The excitation spectra of both complexes become more structured at 77 K , which is particularly noticeable for $\text{Ir}(\text{2-pyppy})_2(\text{acac})$, when compared to its relatively broader spectrum at r.t.

Observed phosphorescence lifetimes of $\text{Ir}(\text{1-pyppy})_2(\text{acac})$ (Table 2) are virtually solvent-independent, with an average value of $2.8\text{ }\mu\text{s}$, which is considered typical for a cyclometalated Ir complex with low energy ^3LC emission. Interestingly, the PLQY increases with solvent polarity, which is a result of a shorter pure radiative lifetime, τ_0 , in more polar solvents. The nonradiative decay rate (k_{nr}) is, however, independent of solvent polarity. In contrast, the observed lifetime of $\text{Ir}(\text{2-pyppy})_2(\text{acac})$ varies significantly with the solvent environment, being almost five times longer in toluene than in acetonitrile. Indeed, the observed lifetimes in toluene ($52.9\text{ }\mu\text{s}$) and in EPA at r.t. ($67.1\text{ }\mu\text{s}$) are more than 20 times longer than for the other isomer, and are extraordinarily long, compared to other common neutral cyclometalated iridium complexes, although not quite as long as some charged complexes recently reported by Zhao and co-workers⁶³ and Nazeeruddin and co-workers⁶⁴ that have lifetimes of 68 and $84\text{ }\mu\text{s}$, respectively. The PLQY values are also approximately an order of magnitude greater than those of $\text{Ir}(\text{1-pyppy})_2(\text{acac})$. These two observations are consistent with the energy gap law in which k_{nr} is greater for the lower-energy-emitting species.^{65,66} The long pure radiative lifetimes of both complexes are hypothesized to be a consequence of the small Ir contribution to the $T_1 \rightarrow S_0$ transitions, which, in combination with the small orbital change associated with the localized $^3\text{LC}/^3\text{ILCT}$ nature of these transitions, leads to a small degree of SOC (similar to the rationalization of the low radiative rate of some $\text{Ru}(\text{II})$ ⁶⁷ and $\text{Ir}(\text{III})$ ⁶⁸ complexes with ^3LC transitions on π -extended ligands). The solvent dependence of τ_0 may be a result of changing the configurational mixing of ^3LC , $^3\text{ILCT}$ and the very minor $^3\text{MLCT}$ contributions to include more charge transfer (of either type, stabilized by more polar solvents), facilitating a slight increase in SOC, making the transition more-allowed in more-polar solvents. In addition, it is suggested that the strain induced by the twist in the cyclometalated ligand of $\text{Ir}(\text{1-pyppy})_2(\text{acac})$ may provide an additional low-energy vibrational deactivation pathway that further increases k_{nr} . Steric crowding has been implicated in increasing k_{nr} for other polyaromatic hydrocarbon-based cyclometalating ligands, although, in these examples, the interaction is between a pendant phenyl group and a pyridyl moiety, rather than with the cyclometalated ring as found here.⁶⁹ Ruthenium complexes with bipyrimidine ligands have been shown to exhibit a similar phenomenon.⁷⁰

Table 2. Photophysical Data for the Complexes Ir(1-pyppy)₂(acac) and Ir(2-pyppy)₂(acac)

IrL ₂ (acac) L	λ_{abs} (nm) ($\log(\epsilon \text{ (M}^{-1} \text{ cm}^{-1}))$) ^{a,b}	solvent ^c	λ_{em} (nm) ^{b,d}	τ (μs) ^e	Φ ^f	τ_0 (ms) ^g	k_r (s ⁻¹) ^h	k_{nr} (s ⁻¹) ⁱ
1-pyppy	272 (4.55), 309 (4.60), 386 (sh. 4.51), 404 (4.58), 423 (sh. 4.40), 519 (3.55)	toluene	684*, 734 (sh.)	2.5	0.0013	1.9	520	4.0×10^5
		CH ₂ Cl ₂	680*, 734 (sh.)	2.7	0.0056	0.48	2100	3.7×10^5
		MeCN	680*, 734 (sh.)	2.5	0.0088	0.28	3600	4.0×10^5
		EPA	680*, 738	3.6				
		EPA (77 K)	679*, 745	5.1				
2-pyppy	274 (4.98), 296 (4.97), 321 (4.95), 411 (4.45), 432 (4.54), 464 (3.99), 493 (3.82)	toluene	626*, 680	52.9	0.021	2.5	400	1.9×10^4
		CH ₂ Cl ₂	626*, 683	37.0	0.063	0.59	1700	2.5×10^4
		MeCN	623*, 685	11.6	0.060	0.19	5200	8.1×10^4
		EPA	623*, 685	67.1				
		EPA (77 K)	622*, 636 (sh.), 676, 692	125				

^aMeasured in CH₂Cl₂ solution. ^bsh. = shoulder. ^cDegassed samples. 298 K, except where stated otherwise. EPA is the solvent mixture 5:5:2 diethyl ether:2-methylbutane:ethanol. ^dExcitation at 400 and 430 nm for Ir(1-pyppy)₂(acac) and Ir(2-pyppy)₂(acac), respectively. Starred value is the emission maximum. ^eExcitation at 337 nm. Decay monitored at 680 and 630 nm for Ir(1-pyppy)₂(acac) and Ir(2-pyppy)₂(acac), respectively. Estimated error: 5% of the value. ^fEstimated error: 10% of the value. ^g $\tau_0 = \tau\Phi_T/\Phi$ and assuming the quantum yield of triplet formation, $\Phi_T = 1$. ^h $k_r = 1/\tau_0$. ⁱ $k_{\text{nr}} = 1/\tau - k_r$.

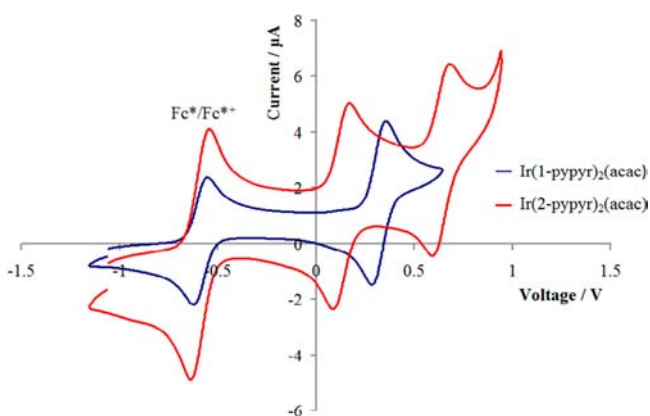


Figure 7. Room-temperature cyclic voltammograms of Ir(1-pyppy)₂(acac) and Ir(2-pyppy)₂(acac) in N₂ saturated 0.1 M [n-Bu₄N]PF₆ CH₂Cl₂ solution at a scan rate of 0.10 V s⁻¹ with all platinum electrodes. Reported vs. Fc/Fc⁺ using the internal reference redox couple Fc*/Fc*⁺ ($E_{1/2} = -0.59$ V vs. Fc/Fc⁺).³⁹

It is worth comparing Ir(1-pyppy)₂(acac) to the previously reported Pt(1-pyppy)₂(acac) complex that has a very similar emission maximum of 680 nm and PLQY of 0.005, but a longer τ of 6.2 μs (i.e., $\tau_0 = 1.2$ ms) in degassed CH₂Cl₂ solution.³¹ This platinum complex was described as having a pyrene-localized excited state, and the similarity of the photophysical data imply the same may be observed here for the Ir complex.

Electrochemical Study. Cyclic voltammetry (CV) of the two complexes was carried out in dry 0.1 M CH₂Cl₂ [n-Bu₄N]PF₆ supporting electrolyte with Fc*/Fc*⁺ as the reference redox couple and are reported relative to the more common Fc/Fc⁺ couple (see experimental section). The recorded voltammograms are shown in Figure 7 and summarized in Table 3 for the range within which redox events were observed. Both isomers exhibit reversible first oxidation waves, with Ir(2-pyppy)₂(acac) showing a second wave (0.64 V) within the solvent window. A second oxidation wave was not observed for Ir(1-pyppy)₂(acac), even when a more strongly interacting electrolyte, [n-Bu₄N]Cl, was used. The difference in anodic and cathodic peaks ($|E_{\text{pc}} - E_{\text{pa}}|$) indicates that all observed oxidations are one electron and are diffusion-controlled under the conditions employed. The first oxidation wave of Ir(1-pyppy)₂(acac) (0.32 V) is shifted

Table 3. Electrochemical Data for Ir(1-pyppy)₂(acac) and Ir(2-pyppy)₂(acac)^a

compound	$E_{1/2}$ (V)	$ E_{\text{pc}} - E_{\text{pa}} $ (mV)
Ir(1-pyppy) ₂ (acac)	0.32	51
Ir(2-pyppy) ₂ (acac)	0.13	56
	0.64	66

^aN₂-saturated CH₂Cl₂/0.1 M [n-Bu₄N]PF₆, r.t., $\nu = 0.10$ V s⁻¹, all platinum electrodes, reported vs. Fc/Fc⁺ using the internal reference redox couple Fc*/Fc*⁺ at $E_{1/2} = -0.59$ V.³⁹

positively by 190 mV, compared to that of Ir(2-pyppy)₂(acac) (0.13 V), indicating a lower-lying HOMO level, assuming that relaxation and electron correlation effects are similar in both compounds. For comparison, Ir(ppy)₂(acac) has an oxidation potential of 0.40 V vs Fc/Fc⁺ when measured under similar conditions.^{54,71} Therefore, the introduction of the pyrenyl moiety has destabilized the HOMO of both isomers of the complexes studied here, to varying extents, relative to Ir(ppy)₂(acac), which contributes in part to the bathochromically shifted absorption and emission. No reduction waves were observed within the solvent window.

Computational Study. Ligands. The cyclometalation of 1-pyppyH with Ir has been described previously as occurring reluctantly; it has therefore necessitated the use of unusual reaction conditions, in particular, the use of trimethyl phosphate as the solvent.³⁰ The 2-pyppyH isomer, however, cyclometalates under conventional conditions, which is an observation that we partially attribute to the greater barrier present for 1-pyppyH to form the required planar conformation for cyclometalation than for 2-pyppyH. The difference in the magnitude of this planarization barrier is manifested in the X-ray crystal structures of the two ligands, in which 2-pyppyH is almost planar, while 1-pyppyH has a dihedral angle of $\sim 41^\circ$ between the pyrene and pyridine moieties. To estimate the size of this barrier, energy calculations stepped around this dihedral angle were performed on both isomers. First, the structures were optimized via DFT calculations at the B3LYP/6-31+G(d) level of theory using the ligand structures obtained from the X-ray crystallographic study as the initial input geometry. This was followed by a scan of the dihedral angle between the pyridine and pyrene rings in 5° steps, with full optimization of

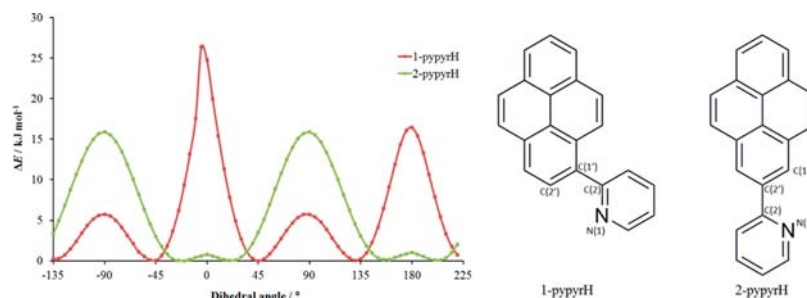


Figure 8. Potential energy surfaces (PES) of 1-pyppyH and 2-pyppyH, showing the difference in total energy, ΔE , as a function of the dihedral angle between the pyrene and pyridine rings. Calculations were performed using DFT at the B3LYP/6-31+G(d) level of theory. To construct these surfaces, the pyrene–pyridine dihedral angles of the two isomers (N(1)–C(2)–C(1′)–C(2′) for 1-pyppyH and N(1)–C(2)–C(2′)–C(1′) for 2-pyppyH, where 0° corresponds to the planar conformations shown), were changed in 5° steps with optimization of all other degrees of freedom. A version of this figure showing the calculated conformations at the various maxima and minima is included in the SI (see Table S2 and Figure S11).

the structure in all other degrees of freedom. From these results, the potential energy surfaces (PES) along this coordinate were constructed and are plotted as the change in total energy from the fully optimized structure as a function of the dihedral angle (see Figure 8). These calculations indicate that, in both isomers, there is an unfavorable steric interaction between the hydrogen atom at the 3-position of the pyridine and the proximal hydrogen atoms of the pyrene rings. For the 2-pyppyH ligand, this energy barrier is calculated to be 0.8 kJ mol^{-1} , while for 1-pyppyH, it is more than 30 times larger at 26 kJ mol^{-1} . Although the minimum energy geometry is calculated for 2-pyppyH at a dihedral angle of 20° , the small planarization barrier can easily be overcome, and a planar geometry is obtained in the crystal structure, similar to that observed in some biphenyl derivatives.⁷² As a consequence of the much larger barrier for 1-pyppyH, the calculated minimum (45°) is in much closer agreement with the 41° dihedral angle found in the crystal structure. It is also observed that the total energy reaches local maxima for both isomers when the two rings are orthogonal (symmetry related -90° and 90° dihedral angles) due to a reduction in conjugation between the rings. In the case of 2-pyppyH, the conjugation must occur via orbitals below the pyrene HOMO, because the nodal plane that passes through the 2-position of the pyrene HOMO (vide infra) prohibits conjugation at any pyrene–pyridine dihedral angle. The compound 1-pyppyH undergoes significant distortion at dihedral angles close to 0° in order to minimize the steric interaction between the hydrogen atoms described above; this has the effect of a less-smooth PES profile around this value. The complex $\text{Ir}(1\text{-pyppy})_2(\text{acac})$ shows an 18° pyrene–pyridine dihedral angle in the crystal structure. Thus, cyclometalation does not fully overcome the barrier, but still represents an $\sim 12 \text{ kJ mol}^{-1}$ increase in energy, compared to the optimized geometry of the uncoordinated ligand. The Boltzmann distribution of the conformers from the calculated PES at the standard cyclometalating temperature of 383 K is included and discussed in Figure S12 in the SI.

For the parent molecule pyrene, the calculated ordering of the two lowest energy singlet excited states, 1L_b (experimentally the lowest energy of the two) and 1L_a , is sensitive to the computational method employed. The use of TD-DFT with the common B3LYP exchange–correlation functional leads to a calculated inversion of states,⁷³ in which the 1L_a state is predicted to lie below the 1L_b state, while the CAM-B3LYP functional achieves the correct state ordering.¹⁹ With this in mind, TD-DFT calculations were performed with both of these

functionals and the 6-31+G(d) basis set, starting from the B3LYP/6-31+G(d) optimized geometry to confirm the assignments made for the experimental UV–visible absorption spectra. For the 2-pyppyH ligand, it is calculated with both methods that the 1L_b is lower in energy than the 1L_a state, as expected, although both the energy difference and oscillator strength of the two states varies with the method (see SI (Tables S3 and S4)). Both methods, however, correctly predict that excitation to the 1L_b state is only weakly allowed ($f \approx 0.01$), similar to other 2-substituted pyrene derivatives¹⁹ and matching the experimentally obtained absorption spectrum. For 1-pyppyH, the ordering of these two states is reversed with both methods, and so the $S_1 \leftarrow S_0$ transition is calculated to be allowed ($f = 0.46\text{--}0.56$) 1L_a state, while $S_2 \leftarrow S_0$ is attributed to the 1L_b state with a very low oscillator strength ($f = 0.001\text{--}0.005$). The 1L_b state is particularly sensitive to substituents in the 1-position and this reversal is often seen in 1-substituted derivatives.¹⁹

Complexes. Geometry optimizations of the ground S_0 and the excited T_1 states of the two Ir complexes were performed using DFT at the B3LYP/6-31G(d)/LANL2DZ level of theory (spin-unrestricted for T_1). Frequency calculations confirmed that minima had been obtained in all cases. Comparison of the bond lengths to the Ir atom experimentally determined by X-ray crystallography with those obtained for the S_0 states by DFT (see Tables S5 and S6 in the SI) show that they are in close agreement, with a maximum/average discrepancy of 2.0%/1.4% and 2.7%/1.9% for $\text{Ir}(1\text{-pyppy})_2(\text{acac})$ and $\text{Ir}(2\text{-pyppy})_2(\text{acac})$, respectively. This difference is a systematic elongation of these bonds by ca. $0.03\text{--}0.06 \text{ \AA}$, as has been observed previously with other calculations at a similar level of theory.⁶⁰ Only minor geometric differences are calculated between the S_0 and T_1 optimized geometries, both in the metal-to-ligand bond lengths ($<0.02 \text{ \AA}$) and in the X–Ir–Y bond angles ($<0.3^\circ$) (X and Y are the C, N and O atoms coordinated to the metal). Furthermore, the calculated geometries are only marginally affected by the inclusion of a high dielectric solvent (MeCN) using the PCM.

Experimentally, the oxidation potential of $\text{Ir}(1\text{-pyppy})_2(\text{acac})$ is 190 mV greater than that of the $\text{Ir}(2\text{-pyppy})_2(\text{acac})$ analogue, and the ordering of the HOMO energies is reproduced here by the calculations, although the calculated energy difference is greater. The HOMO of $\text{Ir}(1\text{-pyppy})_2(\text{acac})$ is distributed over the Ir atom and the single ring of the pyrene system to which it is coordinated and is therefore qualitatively related to the HOMO of $\text{Ir}(\text{ppy})_2(\text{acac})$, which is spread over the metal and

the phenyl ring of the ppy ligand (see the SI (Figure S13) for a comparison). The first oxidation of the parent Ir(ppy)₂(acac) has been ascribed to being predominantly an Ir(III)/Ir(IV) process based on its high level of reversibility and the absence of an oxidation event for the free ligand at a similar potential. The somewhat similar oxidation potentials ($\Delta E_{1/2} = 0.08$ V) and comparable spatial extents of the HOMOs of these two complexes would, upon first inspection, seemingly imply that their first oxidation waves have a similar origin. The HOMO of Ir(2-ppyr)₂(acac) has a much greater pyrenyl component and a much lower oxidation potential than the parent Ir-(ppy)₂(acac) ($\Delta E_{1/2} = 0.27$ V); therefore, its origin is described as a ligand-based oxidation with a small amount of metal character. In order to assign the oxidation processes more conclusively, the structure of the monocations and dications of both complexes were optimized at the same level of theory. However, although these calculations converged and frequency calculations indicated that minima had been located, stability calculations revealed instability in the wave function due to a nonaufbau orbital occupation, which was not immediately obvious from the initial calculations. Enforcing an exchange of the ordering of the orbital pairs associated with the instabilities resulted in new solutions of marginally lower energy; however, frequency calculations indicated that minima had not been found, suggesting that yet-lower energy solutions exist. It was not possible to find solutions that were both stable and provided all-positive frequencies. By considering the orbitals from the different solutions, it was found that very different interpretations of the oxidation procedure could be formulated and thus a definitive description of the oxidation is not available from this method. We therefore urge caution when performing calculations to assign electrochemical data by optimization of the redox products, in particular, advising that both frequency and stability calculations should be routinely run to ensure that erroneous conclusions are not drawn. A more in-depth study of the origin of this problem and an investigation of its generality, as well as efforts to identify a more suitable methodology for these types of calculations, are underway.

In order to gain insight into the observed photophysical properties of the Ir complexes, an analysis of the gas-phase dipole moment changes between the ground and excited states was first undertaken. From the aforementioned optimized neutral geometries, the dipole moments of the S₀ and T₁ states were obtained. Additional single-point energy calculations were performed to evaluate the dipole moment of the triplet state at the ground state geometry, denoted T₁(S₀), and the singlet state at the excited state geometry, S₀(T₁), which correspond to the dipole moments of the Franck–Condon states following absorption and emission, respectively. These data are summarized in Table 4, along with the scalar and vector changes in dipole moment between the optimized S₀ and T₁ states. It can be seen that the scalar change in dipole moment associated with vertical absorption (T₁(S₀) – S₀) is larger for Ir(2-ppyr)₂(acac) than its isomer, indicating a greater degree of charge redistribution following excitation. However, this value is notably smaller than those for chromophores that undergo a significant charge transfer.⁷⁴ Following geometric relaxation to the optimized T₁ geometry, the dipole moment has a value close to that calculated for the optimized ground state, S₀. The magnitudes of both the scalar and vector differences between the dipole moments of the optimized T₁ and S₀ states are small, which is consistent with the lack of solvatochromism in the emission, because only minimal

Table 4. DFT (B3LYP/6-31G(d)/LANL2DZ) Calculated Dipole Moments for the Two Isomeric Complexes in the Gas Phase^a

	calculated dipole moments (debye)	
	Ir(1-ppyr) ₂ (acac)	Ir(2-ppyr) ₂ (acac)
S ₀	1.97	4.76
T ₁	1.74	4.88
T ₁ (S ₀) ^b	3.31	1.12
S ₀ (T ₁) ^c	1.79	4.96
T ₁ (S ₀) – S ₀ ^d	1.34	–3.76
S ₀ (T ₁) – T ₁ ^d	0.05	0.08
T ₁ – S ₀ ^d	–0.23	0.12
T ₁ – S ₀ ^e	1.30	1.08

^aValues obtained from SCF energy calculations. ^bT₁ dipole moment at the S₀ optimized geometry. ^cS₀ dipole moment at the T₁ optimized geometry. ^dScalar change in dipole moment. ^eMagnitude of the vector change in dipole moment. See Table S7 in the SI for vector components.

reorientation of the solvent is required following excitation before emission occurs. The difference in the magnitude of the scalar and vector dipole moment changes is due to a minor deviation from collinearity of the ground and excited state dipole moments (see Table S7 in the SI for vector components). We note that the change in the dipole moment following emission (S₀(T₁) – T₁) is negligible in both cases, indicating even less charge transfer character to the emission than the excitation. The calculated dipole moments were slightly affected in magnitude by the inclusion of MeCN solvent (<1 debye).

TD-DFT calculations were performed using the same functional and mixed basis set, B3LYP/6-31G(d)/LANL2DZ, from the optimized ground state, to calculate excitation energies to the lowest 10 singlet and 10 triplet excited states. Both singlet and triplet transitions are considered important for these materials: the singlet states are expected to produce the highest oscillator strength transitions, but the triplet transitions gain intensity due to the large SOC of the Ir atom, which makes these formally spin-forbidden transitions partially allowed. The lowest energy transitions of both types are summarized in Tables 5 and 6, while the orbitals contributing to these transitions are shown in Table 7. Furthermore, TD-DFT calculations from the S₀ state at the optimized T₁ geometry were used to elucidate the nature of the emission (Tables 5 and 6 provide a summary of the transitions, and Table 8 illustrates the main orbitals involved in these transitions). However, the triplet transition energies calculated for both excitation (T₁ ← S₀) and emission (T₁ → S₀) with this combination of method, functional, and basis set are consistently lower than the experimental band maxima by 0.5–0.6 eV. The lowest-energy singlet excitations, S₁ ← S₀ and S₂ ← S₀, of both isomers are described by LUMO ← HOMO and LUMO+1 ← HOMO transitions and have significant charge-transfer character, being predominantly ¹ILCT, with some additional ¹MLCT character for Ir(1-ppyr)₂(acac). However, the low oscillator strengths, *f* < 0.05, of these transitions make them difficult to identify experimentally, especially since they are expected to overlap with the lower-energy triplet bands. The first singlet excitation to have a significant value of *f* (>0.10) are the S₅ ← S₀ and S₄ ← S₀ transitions for the 1- and 2-substituted isomers, respectively. These transitions are qualitatively more localized, with ¹LC being the dominant descriptor and ¹ILCT being of secondary

Table 5. Lowest-Energy Transitions of Ir(1-pypr)₂(acac) as Calculated by the TD-DFT, TDA, and ΔSCF Methods with the B3LYP and CAM-B3LYP Functionals and the 6-31G(d)/LANL2DZ Basis Set

method	state	transition (<i>f</i>)	<i>E</i> (eV)	λ (nm)	dominant component(s)
Excitation					
TD-DFT B3LYP	1	T ₁ ← S ₀	1.85	674	LUMO ← HOMO–1 LUMO+1 ← HOMO–2
	2	T ₂ ← S ₀	1.85	674	LUMO ← HOMO–2 LUMO+1 ← HOMO–1
	3	T ₃ ← S ₀	2.22	558	LUMO+1 ← HOMO
	4	T ₄ ← S ₀	2.24	554	LUMO ← HOMO
	5	S ₁ ← S ₀ (0.002)	2.49	498	LUMO+1 ← HOMO
	6	S ₂ ← S ₀ (0.045)	2.48	496	LUMO ← HOMO
	13	S ₅ ← S ₀ (0.408)	2.90	428	LUMO ← HOMO–2
	15	S ₆ ← S ₀ (0.171)	2.97	417	LUMO+1 ← HOMO–2 LUMO ← HOMO–1
TD-DFT CAM-B3LYP	1	T ₁ ← S ₀	1.64	756	LUMO+1 ← HOMO–1 LUMO ← HOMO–2
	2	T ₂ ← S ₀	1.64	756	LUMO ← HOMO–1 LUMO+1 ← HOMO–2
	3	T ₃ ← S ₀	2.58	481	LUMO+1 ← HOMO
	4	T ₄ ← S ₀	2.60	477	LUMO ← HOMO
TDA B3LYP	1	T ₁ ← S ₀	2.05	605	LUMO ← HOMO–2 LUMO+1 ← HOMO–1
	2	T ₂ ← S ₀	2.05	605	LUMO ← HOMO–1 LUMO+1 ← HOMO–2
	3	T ₃ ← S ₀	2.24	554	LUMO+1 ← HOMO
	4	T ₄ ← S ₀	2.26	549	LUMO ← HOMO
TDA CAM-B3LYP	1	T ₁ ← S ₀	2.18	569	LUMO+1 ← HOMO–1 LUMO ← HOMO–2
	2	T ₂ ← S ₀	2.18	569	LUMO ← HOMO–1 LUMO+1 ← HOMO–2
	3	T ₃ ← S ₀	2.67	464	LUMO+1 ← HOMO LUMO+1 ← HOMO–2
	4	T ₄ ← S ₀	2.69	461	LUMO ← HOMO LUMO ← HOMO–2
ΔSCF B3LYP		T ₁ (S ₀) – S ₀	2.30	539	
experimental	1	T ₁ ← S ₀	2.39	519	
Emission					
TD-DFT B3LYP ^a	1	T ₁ → S ₀	1.25	992	LUMO → HOMO
TD-DFT CAM-B3LYP ^a	1	T ₁ → S ₀	0.75	1653	LUMO → HOMO
TDA B3LYP ^a	1	T ₁ → S ₀	1.51	821	LUMO → HOMO
TDA CAM-B3LYP ^a	1	T ₁ → S ₀	1.55	805	LUMO → HOMO
ΔSCF B3LYP		T ₁ – S ₀ (T ₁)	1.50	828	
experimental		T ₁ → S ₀	1.82	680	

^aTaken as the reverse of the absorption process calculated from the S₀ state at the T₁ geometry.

importance. The energy difference between the calculated value of these higher-energy transitions and the maxima of the experimentally assigned ¹LC/¹ILCT bands of Ir(1-pypr)₂(acac) and Ir(2-pypr)₂(acac) is 0.17 and 0.03 eV, respectively, representing excellent agreement. In order to identify an alternative method that addressed the greater energy

discrepancies in the triplet transition energies, it was first necessary to consider the nature of the excitation and emission in terms of orbital transitions and classification (³LC versus ³CT) described by these initial calculations; thus, such an analysis is now presented.

Table 6. Lowest-Energy Transitions of Ir(2-pyppy)₂(acac) as Calculated by the TD-DFT, TDA, and ΔSCF Methods with the B3LYP and CAM-B3LYP Functionals and the 6-31G(d)/LANL2DZ Basis Set

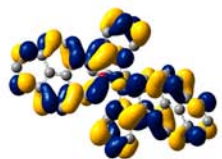
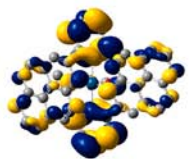

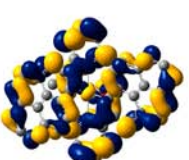
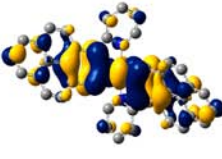
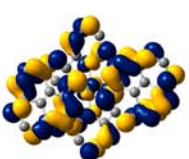
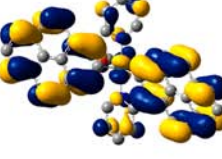
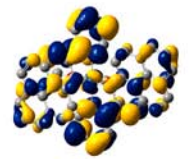
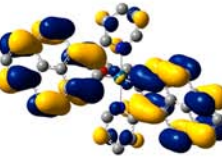

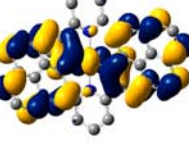
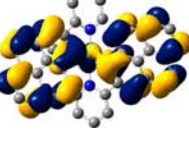
method	state	transition (<i>f</i>)	<i>E</i> (eV)	λ (nm)	dominant component(s)
Excitation					
TD-DFT B3LYP	1	T ₁ ← S ₀	1.99	624	LUMO+2 ← HOMO LUMO+3 ← HOMO−1 LUMO+2 ← HOMO−1
	2	T ₂ ← S ₀	2.04	609	LUMO+3 ← HOMO LUMO+5 ← HOMO
	3	T ₃ ← S ₀	2.13	582	LUMO ← HOMO
	4	T ₄ ← S ₀	2.26	549	LUMO+1 ← HOMO
	5	S ₁ ← S ₀ (0.003)	2.32	534	LUMO ← HOMO
	6	S ₂ ← S ₀ (0.029)	2.50	497	LUMO+1 ← HOMO
	11	S ₄ ← S ₀ (0.144)	2.84	436	LUMO+2 ← HOMO
TD-DFT CAM-B3LYP	1	T ₁ ← S ₀	1.79	693	LUMO+2 ← HOMO LUMO+3 ← HOMO−1
	2	T ₂ ← S ₀	1.81	685	LUMO+3 ← HOMO LUMO+2 ← HOMO−1
	3	T ₃ ← S ₀	2.58	481	LUMO ← HOMO
	4	T ₄ ← S ₀	2.64	470	LUMO+1 ← HOMO LUMO ← HOMO−1
TDA B3LYP	1	T ₁ ← S ₀	2.14	579	LUMO ← HOMO
	2	T ₂ ← S ₀	2.20	564	LUMO+2 ← HOMO LUMO+1 ← HOMO LUMO+3 ← HOMO
	3	T ₃ ← S ₀	2.27	546	LUMO+2 ← HOMO−1 LUMO+5 ← HOMO
	4	T ₄ ← S ₀	2.30	539	LUMO+1 ← HOMO LUMO+2 ← HOMO
TDA CAM-B3LYP	1	T ₁ ← S ₀	2.36	525	LUMO+2 ← HOMO LUMO+3 ← HOMO−1
	2	T ₂ ← S ₀	2.39	519	LUMO+3 ← HOMO LUMO+2 ← HOMO−1
	3	T ₃ ← S ₀	2.66	466	LUMO ← HOMO
	4	T ₄ ← S ₀	2.73	454	LUMO+1 ← HOMO LUMO ← HOMO−1
ΔSCF B3LYP		T ₁ (S ₀) − S ₀	2.27	546	
experimental	1	T ₁ ← S ₀	2.51	493	
Emission					
TD-DFT B3LYP ^a	1	T ₁ → S ₀	1.45	856	LUMO+1 → HOMO LUMO+2 → HOMO
TD-DFT CAM-B3LYP ^a	1	T ₁ → S ₀	1.02	1216	LUMO+1 → HOMO LUMO → HOMO LUMO+2 → HOMO
TDA B3LYP ^a	1	T ₁ → S ₀	1.72	721	LUMO+1 → HOMO LUMO+2 → HOMO
TDA CAM-B3LYP ^a	1	T ₁ → S ₀	1.77	700	LUMO+1 → HOMO LUMO → HOMO LUMO+2 → HOMO
ΔSCF B3LYP		T ₁ − S ₀ (T ₁)	1.70	729	
experimental	1	T ₁ ← S ₀	1.99	623	

^aTaken as the reverse of the absorption process calculated from the S₀ state at the T₁ geometry.

Excitation to the T₁ state of both isomers involves a transition from orbitals based on the pyrene moiety, with some metal contribution, to one additionally incorporating the pyridine ring. This is similar to that calculated for Ir(ppy)₂(bza) (bzaH = benzoylacetone),⁶⁰ although there is a much greater contribution from the pyrene ring in the excited state, compared to the analogous phenyl ring in Ir(ppy)₂(bza). Specifically, for Ir(1-pyppy)₂(acac), T₁ and T₂ are quasi-degenerate and are described by a transition between the

quasi-degenerate pairs HOMO−1 and HOMO−2 to LUMO and LUMO+1 (the molecule belongs to the point group C₂ that precludes truly degenerate orbitals). Each of these orbitals contains a nodal plane along the long axis of the pyrene ring through the site of coordination to the iridium, and so there is only a small metal contribution to the transition. Interestingly, the HOMO, which is not involved in the transition, does not contain this nodal plane. For Ir(2-pyppy)₂(acac), T₁ and T₂ are further separated in energy and involve transitions from

Table 7. Frontier and Other Orbitals That Contribute to the Lowest-Energy Excitations of Ir(1-pyppy)₂(acac) and Ir(2-pyppy)₂(acac) as Calculated by DFT at the B3LYP/6-31G(d)/LANL2DZ Level of Theory for the Optimized S₀ States^a

orbital (<i>E</i> (eV))	Ir(1-pyppy) ₂ (acac)	orbital (<i>E</i> (eV))	Ir(2-pyppy) ₂ (acac)
LUMO+1 (-2.10)		LUMO+5 (-0.84)	
LUMO (-2.11)		LUMO+3 (-1.08)	
HOMO (-5.14)		LUMO+2 (-1.18)	
HOMO-1 (-5.28)		LUMO+1 (-1.40)	
HOMO-2 (-5.29)		LUMO (-1.58)	
		HOMO (-4.47)	
		HOMO-1 (-4.86)	

^aIsovalue: $\pm 0.02 [e a_0^{-3}]^{1/2}$. Hydrogen atoms are omitted for the sake of clarity.

HOMO and HOMO-1 to LUMO+2 and LUMO+3. These orbitals have a nodal plane along the long axis of the pyrene ring that reduces intraligand conjugation between the pyridine and pyrene moieties. This is contrary to Ir(1-pyppy)₂(acac), which is conjugated between these two rings, resulting in a calculated 0.15 eV (50 nm) lower energy transition to the T₁ state. This is in agreement with the observed bathochromic shift of the lowest energy absorption band and the emission maximum for this isomer. The best description of the excited state of both of these isomers is an admixture of ³LC, ³ILCT, and ³MLCT transitions. For Ir(1-pyppy)₂(acac), this admixture has ³LC (on the pyrene moiety) as the dominant factor, with ³ILCT (between the pyrene and pyridine rings) playing a

secondary role. Conversely, Ir(2-pyppy)₂(acac) has somewhat greater ³ILCT character to the excitation, with ³LC being less important to the description. This is consistent with the calculated larger change in dipole moment upon excitation for Ir(2-pyppy)₂(acac), indicative of more charge-transfer character. In both complexes, ³MLCT is much less important, although some small component must be included for a full description. This correlates well with our explanation of the observed photophysical measurements.

The higher-energy T₃ ← S₀ and T₄ ← S₀ transitions of both complexes are predominantly ³ILCT, with some additional ³MLCT character for Ir(1-pyppy)₂(acac). The orbital description of these transitions is similar to that of the low-energy

Table 8. Frontier and Other Orbitals That Contribute to the Emission of Ir(1-pyppy)₂(acac) and Ir(2-pyppy)₂(acac) as Calculated by DFT at the B3LYP/6-31G(d)/LANL2DZ Level of Theory for the S₀ States at the T₁ Optimized Geometries^a

orbital (<i>E</i> (eV))	Ir(1-pyppy) ₂ (acac)	orbital (<i>E</i> (eV))	Ir(2-pyppy) ₂ (acac)
LUMO (-2.09)		LUMO+2 (-1.32)	
HOMO (-4.78)		LUMO+1 (-1.46)	
		LUMO (-1.59)	
		HOMO (-4.31)	

^aIsovalue: $\pm 0.02 [e a_0^{-3}]^{1/2}$. Hydrogen atoms are omitted for the sake of clarity.

singlet transitions, $S_1 \leftarrow S_0$ and $S_2 \leftarrow S_0$, which have low oscillator strength; therefore, these related triplet transitions are expected to have vanishingly small oscillator strengths and are not expected to be experimentally observable. The $T_1 \leftarrow S_0$ and $T_2 \leftarrow S_0$ would be expected to have relatively higher oscillator strengths as their character is more akin to the higher oscillator strength singlet states discussed above; although, of course, their triplet nature makes them significantly weaker than the related singlet transitions.

Spin-density plots of the T₁ states were constructed and are included in Figure 9 (gas phase). Little difference is observable

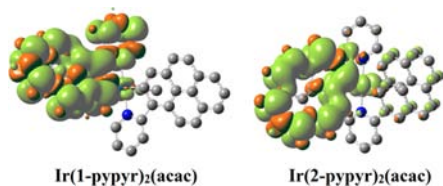


Figure 9. Surface plots of the spin-density distribution of the optimized T₁ states of Ir(1-pyppy)₂(acac) and Ir(2-pyppy)₂(acac). Calculated using DFT at the UB3LYP/6-31G(d)/LANL2DZ level. Isovalue: $\pm 5 \times 10^{-4} e a_0^{-3}$. Hydrogen atoms are omitted for the sake of clarity.

when MeCN solvent is included in the calculation through the PCM. From these plots, it can be seen that, following geometric relaxation, the excited state becomes localized on the Ir atom and on a single cyclometalated ligand, as has been seen previously in other derivatives.⁷⁵ In the case of Ir(1-pyppy)₂(acac), the ligand component is delocalized over the conjugated pyridyl and pyrenyl moieties, while for Ir(2-pyppy)₂(acac), it is localized on the pyrene ring. Ir(1-

pyppy)₂(acac) undergoes emission that can be described by a LUMO \rightarrow HOMO transition (orbitals used here refer to the S₀ state at the T₁ optimized geometry), which is almost purely ³LC delocalized over both the conjugated pyrenyl and pyridyl components. This is consistent with the observed long pure radiative lifetime in which there is little orbital momentum change and only a small metal contribution to the transition. Ir(2-pyppy)₂(acac) exhibits a much more mixed emissive state, with a combination of ³LC and ³ILCT characters. We note that, for this isomer, a LUMO \rightarrow HOMO component would be almost purely ³ILCT, but this is considered to provide only a minor contribution to the transition, and therefore mixed ³LC/³ILCT offers the best description of the emitting state. Furthermore, the pyrene components of the orbitals involved in the emission of both complexes are pyrene-like, that is the HOMO of both complexes in the T₁ geometry resemble the HOMO of pyrene, and the LUMO of Ir(1-pyppy)₂(acac) and the LUMO+1 and LUMO+2 of Ir(2-pyppy)₂(acac) resemble a distorted version of the LUMO of pyrene. Therefore, the pyrene ³LC component is a pseudo-³L_a transition.

The assignment of mixed ³LC/³ILCT character for the lowest energy triplet states of both isomers raised two potential issues that were addressed separately. Recently, a connection between a near triplet instability in the ground state wave function and an artificial lowering of triplet transitions calculated by TD-DFT using functionals with a significant Hartree–Fock (HF) exchange component has been identified.⁴⁶ This effect is particularly important for transitions having significant spatial overlap of the ground and excited state, such as ³LC transitions. B3LYP, the functional initially employed here, contains 20% HF exchange and thus would be susceptible to this problem if a near instability existed; therefore, stability calculations were conducted and the calculated eigenvalues,

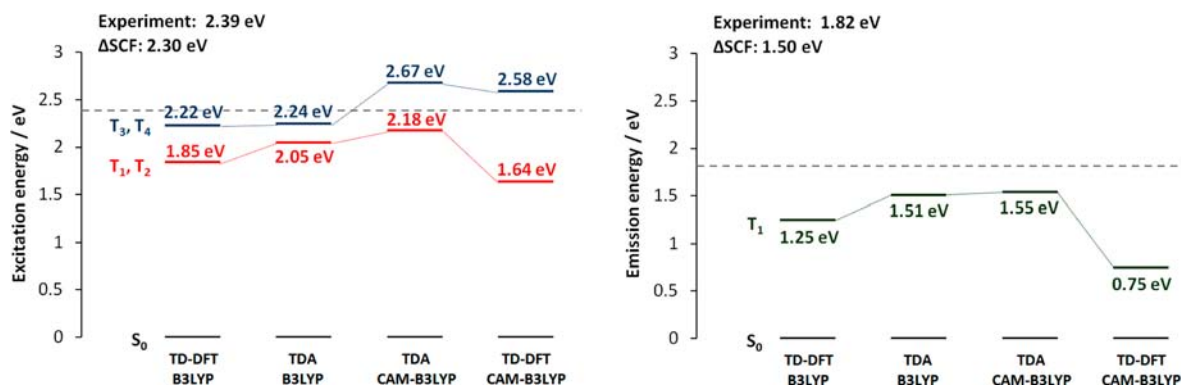


Figure 10. Comparison of the calculated excitation (left) and emission (right) transition energies for Ir(1-pyppy)₂(acac) using the TD-DFT and TDA methods with the B3LYP and CAM-B3LYP exchange-correlation functionals. The mixed 6-31G(d)/LANL2DZ basis set was used in each case. Experimental values are indicated by dashed lines. Energy labels for excitation are those calculated for the T₁ ← S₀ (red) and T₃ ← S₀ (blue) transitions, as defined from the initial TD-DFT/B3LYP calculation.

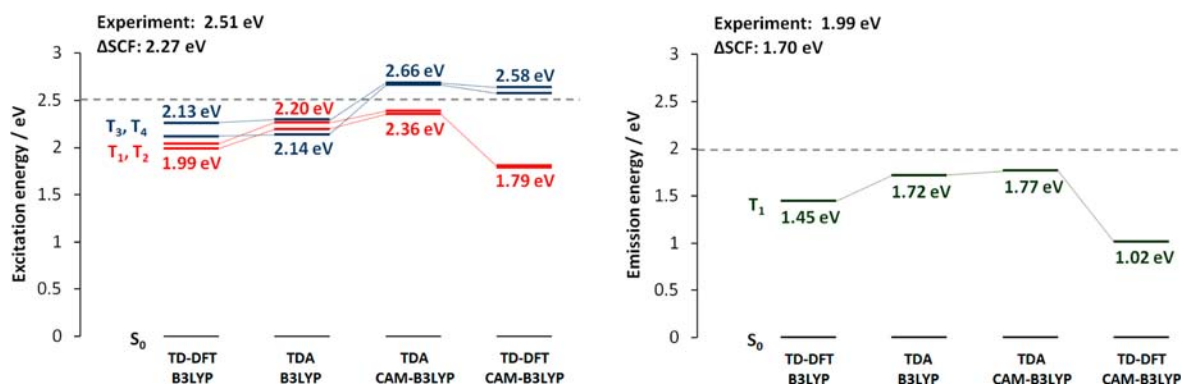


Figure 11. Comparison of the calculated excitation (left) and emission (right) transition energies for Ir(2-pyppy)₂(acac) using the TD-DFT and TDA methods with the B3LYP and CAM-B3LYP exchange-correlation functionals. The mixed 6-31G(d)/LANL2DZ basis set was used in each case. Experimental values are indicated by dashed lines. Energy labels for excitation are those calculated for the T₁ ← S₀ (red) and T₃ ← S₀ (blue) transitions, as defined from the initial TD-DFT/B3LYP calculation.

ω_{STAB} were assessed. The eigenvectors from these calculations can be associated with particular transitions from the TD-DFT calculations, because they are similarly described by transitions between pairs of orbitals. It has been found previously that, empirically, a value of $\omega_{\text{STAB}} < 2$ eV is an indicator of this problem with HF exchange-containing functionals.⁴⁷ The lowest triplet transitions of both complexes were found to have ω_{STAB} values that conform to this criterion. It has also been identified that a solution to this error is provided by the Tamm-Dancoff Approximation (TDA) to TD-DFT.⁴⁷ In conventional TD-DFT, a combination of both excitation and de-excitation between orbital pairs is used to describe a transition and, while mathematically rigorous, this can lead to underestimation of, in particular, localized triplet transitions. The TDA method sets the matrix elements responsible for the de-excitation components to zero, providing a more physically intuitive solution and also partially correcting the underestimation of the transition energies.

Performing TDA calculations (B3LYP/6-31G(d)/LANL2DZ) improved the correspondence between theory and experiment to 0.34 and 0.37 eV for Ir(1-pyppy)₂(acac) and Ir(2-pyppy)₂(acac), respectively (Figures 10 and 11); similarly, emission energies were improved, and are within 0.27–0.31 eV of the experimental value with this method. Next, considering that the T₁ ← S₀ and T₂ ← S₀ transitions have some ³ILCT character, the CAM-B3LYP functional was selected, because of

its better description of CT.^{48,76} This functional incorporates a variable (distance-dependent) amount of HF exchange, rather than the fixed 20% included in B3LYP. Combining TDA calculations with the CAM-B3LYP functional and the same 6-31G(d)/LANL2DZ basis set provided further improvement, with calculated energies within 0.21 and 0.15 eV of the experimental values for Ir(1-pyppy)₂(acac) and Ir(2-pyppy)₂(acac), respectively. However, due to, and supporting, the assignment of the emission as being nearly pure ³LC, TDA with the CAM-B3LYP functional provided only a very modest improvement over TDA with B3LYP in the emission values ($\Delta E = 0.04$ – 0.05 eV). The residual difference between the experimental and theoretical values is justified by the relatively small basis set, the small perturbation expected upon inclusion of solvent and the nonequivalence of the compared values (vertical gas phase compared to the band maximum that may not correspond to the $\nu = 0'' \leftarrow 0'$ transition). Noticeably, when only the correction to the long-range component was performed, that is the CAM-B3LYP functional was used with conventional TD-DFT, a large detrimental effect is observed, with excitation values being ca. 0.7 eV and emission values ca. 1.0–1.1 eV lower than experiment. This can be rationalized based on the larger HF exchange component of CAM-B3LYP, exacerbating the near triplet instability problem of the local transition component to a greater extent than the CT component is corrected.

The $T_3 \leftarrow S_0$ and $T_4 \leftarrow S_0$ transitions are of much greater charge-transfer character and so the transition energies are only marginally affected by the use of the TDA method with B3LYP, while CAM-B3LYP with either TDA or TD-DFT leads to an increase in energy as the long-range problem is corrected. Indeed, in the case of $\text{Ir}(2\text{-ppypr})_2(\text{acac})$, the difference in the response of the more localized (T_1 and T_2) and more CT (T_3 and T_4) states to the choice of method leads to a change in state order when TDA/B3LYP is used compared to TD-DFT/B3LYP, which shows that the other low-lying states must be considered when choosing a method in order to avoid incorrect state ordering. It is important to note that the orbital pairs describing the transitions provided by the different methods are similar, while the energies are significantly affected, thus our interpretations of the nature of the transitions, based on the initial TD-DFT/B3LYP calculations, are unaffected. This study thus highlights the need for very careful selection of both the computational method and functional when performing calculations to assess the photophysical properties of phosphorescent organometallic complexes, especially where there is mixed character to the transition. Of particular practical importance is that the TDA/CAM-B3LYP combination is of a similar computational cost to TD-DFT/B3LYP with the same basis set, but greatly increases the correspondence in transition energies between theory and experiment in this case. This method will likely be useful for similar complexes when TD-DFT methods with the B3LYP functional predict very low, or even imaginary, values of the transition energies.⁷⁷

The ΔSCF method was also evaluated as an alternative to TD-DFT, taking for excitation the energy difference between the optimized S_0 geometry and the T_1 state at the S_0 geometry ($S_0 - T_1(S_0)$) and for emission, the energy difference between the T_1 optimized geometry and the S_0 state at the T_1 geometry ($T_1 - S_0(T_1)$). This method is found to give reasonable agreement with experiment, although, in most cases, slightly worse than the TDA/CAM-B3LYP combination. The ΔSCF method has recently gained renewed interest as a computationally low-cost alternative to TD-DFT with some theoretical justification as the exact solution in the adiabatic limit, although the method often relies heavily on cancellation of errors;⁷⁸ therefore, the TDA/CAM-B3LYP approach, which is on arguably firmer theoretical grounding, presents itself as the best method for use with this system and should be considered for other similar compounds.

CONCLUSIONS

Two isomeric cyclometalated iridium complexes have been synthesized to investigate the impact of varying the coordination site on the photophysics of pyrene-derived cyclometalating ligands. The greatest factor differentiating the two isomers appears to be the location of the nodal plane along the long axis of pyrene and whether this reduces orbital overlap between the metal and the ligand or intraligand between the pyridine and pyrene rings. It is found that both isomers exhibit predominantly LC lowest-energy triplet excitations with some ILCT character, which are sensitive to solvent environment in terms of their observed and pure radiative lifetimes and quantum yields, but do not show solvatochromism in their emission spectra. Lifetime and quantum yield measurements made on this class of material are typically performed in a single solvent, whereas herein, we show that further effects may be observed when a range of solvents is employed. In addition, crystallographic and DFT analysis has provided a rationale for

the more unusual conditions required for the cyclometalation of 1-ppyprH compared to 2-ppyprH, based on an unfavorable steric interaction in the former. The unfavorable steric interaction present in $\text{Ir}(1\text{-ppypr})_2(\text{acac})$ is also believed to promote nonradiative deactivation through an additional vibrational mode, enhancing k_{nr} for this isomer. DFT, TD-DFT, TDA, and ΔSCF calculations have been used to interpret the observed photophysical data, such as the red-shifted absorption of $\text{Ir}(1\text{-ppypr})_2(\text{acac})$. In addition, these calculations have confirmed that excitation to the lowest-energy excited state for both complexes is a mixed ${}^3\text{ILCT}/{}^3\text{LC}$ -type transition with only minor ${}^3\text{MLCT}$ character, while the emission is almost purely ${}^3\text{LC}$ for $\text{Ir}(1\text{-ppypr})_2(\text{acac})$ with some additional ${}^3\text{ILCT}$ character for $\text{Ir}(2\text{-ppypr})_2(\text{acac})$, a finding that is consistent with the measured photophysical data. We find that the TDA method employing the CAM-B3LYP functional is an effective combination for the calculation of the excitation and emission energies of these phosphorescent iridium complexes that have mixed excited state character. The main general conclusion that can be drawn from this combined theoretical and experimental analysis of the photophysical and electrochemical data of these two isomeric complexes is that assignment by analogy with the parent complex $\text{Ir}(\text{ppy})_2(\text{acac})$ is not always reliable for new $\text{IrL}_2(\text{acac})$ complexes, even when, superficially, the experimental data look similar and, therefore, each new system should be evaluated individually.

ASSOCIATED CONTENT

Supporting Information

X-ray crystallographic data of 1-ppyprH, 2-ppyprH, $\text{Ir}(1\text{-ppypr})_2(\text{acac})$, and $\text{Ir}(2\text{-ppypr})_2(\text{acac})$ in CIF format. Crystal packing diagrams of 1-ppyprH and 2-ppyprH. Additional computational details. NMR spectra of all compounds. This material is available free of charge via the Internet at <http://pubs.acs.org>.

AUTHOR INFORMATION

Corresponding Author

*Tel.: + 44 (0) 191 33 42023. E-mail: andrew.beeby@durham.ac.uk

Present Address

[§]Institut für Anorganische Chemie, Julius-Maximilians-Universität Würzburg, Am Hubland, 97074 Würzburg, Germany.

Notes

The authors declare no competing financial interest.

ACKNOWLEDGMENTS

R.M.E. thanks Durham University for funding through a Durham Doctoral Fellowship. K.F. and M.J.G.P. thank the EPSRC for funding. We are grateful to the reviewers for helpful suggestions.

REFERENCES

- (1) Baldo, M. A.; Thompson, M. E.; Forrest, S. R. *Nature* **2000**, *403*, 750.
- (2) Nazeeruddin, M. K.; Humphry-Baker, R.; Berner, D.; Rivier, S.; Zuppiroli, L.; Grätzel, M. *J. Am. Chem. Soc.* **2003**, *125*, 8790.
- (3) Yang, C.-H.; Cheng, Y.-M.; Chi, Y.; Hsu, C.-J.; Fang, F.-C.; Wong, K.-T.; Chou, P.-T.; Chang, C.-H.; Tsai, M.-H.; Wu, C.-C. *Angew. Chem., Int. Ed.* **2007**, *46*, 2418.
- (4) Tsuboyama, A.; Iwawaki, H.; Furugori, M.; Mukaide, T.; Kamatani, J.; Igawa, S.; Moriyama, T.; Miura, S.; Takiguchi, T.; Okada, S.; Hoshino, M.; Ueno, K. *J. Am. Chem. Soc.* **2003**, *125*, 12971.

- (5) Lamansky, S.; Djurovich, P.; Murphy, D.; Abdel-Razzaq, F.; Lee, H.-E.; Adachi, C.; Burrows, P. E.; Forrest, S. R.; Thompson, M. E. *J. Am. Chem. Soc.* **2001**, *123*, 4304.
- (6) Flamigni, L.; Barbieri, A.; Sabatini, C.; Ventura, B.; Barigelletti, F. *Top. Curr. Chem.* **2007**, *281*, 143.
- (7) Lowry, M. S.; Bernhard, S. *Chem.—Eur. J.* **2006**, *12*, 7970.
- (8) You, Y.; Park, S. Y. *J. Am. Chem. Soc.* **2005**, *127*, 12438.
- (9) Zhou, G.; Ho, C.-L.; Wong, W.-Y.; Wang, Q.; Ma, D.; Wang, L.; Lin, Z.; Marder, T. B.; Beeby, A. *Adv. Funct. Mater.* **2008**, *18*, 499.
- (10) Hofbeck, T.; Yersin, H. *Inorg. Chem.* **2010**, *49*, 9290.
- (11) Steunenberg, P.; Ruggi, A.; van den Berg, N. S.; Buckle, T.; Kuil, J.; van Leeuwen, F. W. B.; Velders, A. H. *Inorg. Chem.* **2012**, *51*, 2105.
- (12) Mayo, E. I.; Kils, K.; Tirrell, T.; Djurovich, P. I.; Tamayo, A.; Thompson, M. E.; Lewis, N. S.; Gray, H. B. *Photochem. Photobiol. Sci.* **2006**, *5*, 871.
- (13) Fihri, A.; Artero, V.; Pereira, A.; Fontecave, M. *Dalton Trans.* **2008**, 5567.
- (14) You, Y.; Park, S. Y. *Dalton Trans.* **2009**, 1267.
- (15) Nakajima, A. *Bull. Chem. Soc. Jpn.* **1973**, *46*, 2602.
- (16) Birks, J. B.; Dyson, D. J.; Munro, I. H. *Proc. R. Soc. London, Ser. A* **1963**, *275*, 575.
- (17) Karpovich, D. S.; Blanchard, G. J. *J. Phys. Chem.* **1995**, *99*, 3951.
- (18) Figueira-Duarte, T. M.; Müllen, K. *Chem. Rev.* **2011**, *111*, 7260.
- (19) Crawford, A. G.; Dwyer, A. D.; Liu, Z.; Steffen, A.; Beeby, A.; Pålsson, L.-O.; Tozer, D. J.; Marder, T. B. *J. Am. Chem. Soc.* **2011**, *133*, 13349.
- (20) Leslie, W.; Poole, R. A.; Murray, P. R.; Yellowlees, L. J.; Beeby, A.; Williams, J. A. G. *Polyhedron* **2004**, *23*, 2769.
- (21) Pomestchenko, I. E.; Luman, C. R.; Hissler, M.; Ziessel, R.; Castellano, F. N. *Inorg. Chem.* **2003**, *42*, 1394.
- (22) Kozlov, D. V.; Tyson, D. S.; Goze, C.; Ziessel, R.; Castellano, F. N. *Inorg. Chem.* **2004**, *43*, 6083.
- (23) Goze, C.; Sabatini, C.; Barbieri, A.; Barigelletti, F.; Ziessel, R. *Inorg. Chem.* **2007**, *46*, 7341.
- (24) Spaenig, F.; Olivier, J.-H.; Prusakova, V.; Retailleau, P.; Ziessel, R.; Castellano, F. N. *Inorg. Chem.* **2011**, *50*, 10859.
- (25) Constable, E. C.; Neuburger, M.; Rösel, P.; Schneider, G. E.; Zampese, J. A.; Housecroft, C. E.; Monti, F.; Armaroli, N.; Costa, R. D.; Ortí, E. *Inorg. Chem.* **2012**, *52*, 885.
- (26) Heng, W. Y.; Hu, J.; Yip, J. H. K. *Organometallics* **2007**, *26*, 6760.
- (27) Gao, L.; Peay, M. A.; Partyka, D. V.; Updegraff, J. B.; Teets, T. S.; Esswein, A. J.; Zeller, M.; Hunter, A. D.; Gray, T. G. *Organometallics* **2009**, *28*, 5669.
- (28) Bonnefous, C.; Chouai, A.; Thummel, R. P. *Inorg. Chem.* **2001**, *40*, 5851.
- (29) Hu, J.; Yip, J. H. K.; Ma, D.-L.; Wong, K.-Y.; Chung, W.-H. *Organometallics* **2008**, *28*, 51.
- (30) Ionkin, A. S.; Marshall, W. J.; Fish, B. M. *Organometallics* **2006**, *25*, 1461.
- (31) Wu, W. T.; Wu, W. H.; Ji, S. M.; Guo, H. M.; Zhao, J. Z. *Eur. J. Inorg. Chem.* **2010**, 4470.
- (32) Lee, W.; Kwon, T.-H.; Kwon, J.; Kim, J.-Y.; Lee, C.; Hong, J.-I. *New J. Chem.* **2011**, *35*, 2557.
- (33) Vyas, P. V.; Bhatt, A. K.; Ramachandriah, G.; Bedekar, A. V. *Tetrahedron Lett.* **2003**, *44*, 4085.
- (34) Crawford, A. G.; Liu, Z.; Mkhaliid, I. A. I.; Thibault, M.-H.; Schwarz, N.; Alcaraz, G.; Steffen, A.; Collings, J. C.; Batsanov, A. S.; Howard, J. A. K.; Marder, T. B. *Chem.—Eur. J.* **2012**, *18*, 5022.
- (35) Coventry, D. N.; Batsanov, A. S.; Goeta, A. E.; Howard, J. A. K.; Marder, T. B.; Perutz, R. N. *Chem. Commun.* **2005**, 2172.
- (36) Batsanov, A. S.; Howard, J. A. K.; Albesa-Jové, D.; Collings, J. C.; Liu, Z.; Mkhaliid, I. A. I.; Thibault, M.-H.; Marder, T. B. *Cryst. Growth Des.* **2012**, *12*, 2794.
- (37) Bianchini, C.; Gatteschi, D.; Giambastiani, G.; Guerrero Rios, I.; Ienco, A.; Laschi, F.; Mealli, C.; Meli, A.; Sorace, L.; Toti, A.; Vizza, F. *Organometallics* **2007**, *26*, 726.
- (38) Porrès, L.; Holland, A.; Pålsson, L.-O.; Monkman, A. P.; Kemp, C.; Beeby, A. *J. Fluoresc.* **2006**, *16*, 267.
- (39) Connelly, N. G.; Geiger, W. E. *Chem. Rev.* **1996**, *96*, 877.
- (40) Frisch, M. J.; Trucks, G. W.; Schlegel, H. B.; Scuseria, G. E.; Robb, M. A.; Cheeseman, J. R.; Scalmani, G.; Barone, V.; Mennucci, B.; Petersson, G. A.; Nakatsuji, H.; Caricato, M.; Li, X.; Hratchian, H. P.; Izmaylov, A. F.; Bloino, J.; Zheng, G.; Sonnenberg, J. L.; Hada, M.; Ehara, M.; Toyota, K.; Fukuda, R.; Hasegawa, J.; Ishida, M.; Nakajima, T.; Honda, Y.; Kitao, O.; Nakai, H.; Vreven, T.; Montgomery, J. A.; Peralta, J. E.; Ogliaro, F.; Bearpark, M.; Heyd, J. J.; Brothers, E.; Kudin, K. N.; Staroverov, V. N.; Kobayashi, R.; Normand, J.; Raghavachari, K.; Rendell, A.; Burant, J. C.; Iyengar, S. S.; Tomasi, J.; Cossi, M.; Rega, N.; Millam, J. M.; Klene, M.; Knox, J. E.; Cross, J. B.; Bakken, V.; Adamo, C.; Jaramillo, J.; Gomperts, R.; Stratmann, R. E.; Yazyev, O.; Austin, A. J.; Cammi, R.; Pomelli, C.; Ochterski, J. W.; Martin, R. L.; Morokuma, K.; Zakrzewski, V. G.; Voth, G. A.; Salvador, P.; Dannenberg, J. J.; Dapprich, S.; Daniels, A. D.; Farkas, Foresman, J. B.; Ortiz, J. V.; Cioslowski, J.; Fox, D. J. *Gaussian 09, Revision A.1*; Wallingford, CT, 2009.
- (41) Shao, Y.; Fusti-Molnar, L.; Jung, Y.; Kussmann, J.; Ochsenfeld, C.; Brown, S. T.; Gilbert, A. T. B.; Slipchenko, L. V.; Levchenko, S. V.; O'Neill, D. P.; DiStasio, R. A., Jr; Lochan, R. C.; Wang, T.; Beran, G. J. O.; Besley, N. A.; Herbert, J. M.; Lin, C. Y.; Van Voorhis, T.; Chien, S.-H.; Sodt, A.; Steele, R. P.; Rassolov, V. A.; Maslen, P. E.; Korambath, P. P.; Adamson, R. D.; Austin, B.; Baker, J.; Byrd, E. F. C.; Dachsel, H.; Doerksen, R. J.; Dreuw, A.; Dunietz, B. D.; Dutoi, A. D.; Furlani, T. R.; Gwaltney, S. R.; Heyden, A.; Hirata, S.; Hsu, C.-P.; Kedziora, G.; Khalliulin, R. Z.; Klunzinger, P.; Lee, A. M.; Lee, M. S.; Liang, W.; Lotan, I.; Nair, N.; Peters, B.; Proynov, E. I.; Pieniazek, P. A.; Rhee, Y. M.; Ritchie, J.; Rosta, E.; Sherrill, C. D.; Simmonett, A. C.; Subotnik, J. E.; Woodcock, H. L., III; Zhang, W.; Bell, A. T.; Chakraborty, A. K.; Chipman, D. M.; Keil, F. J.; Warshel, A.; Hehre, W. J.; Schaefer, H. F., III; Kong, J.; Krylov, A. I.; Gill, P. M. W.; Head-Gordon, M. *Phys. Chem. Chem. Phys.* **2006**, *8*, 3172.
- (42) Becke, A. D. *J. Chem. Phys.* **1993**, *98*, 5648.
- (43) Lee, C.; Yang, W.; Parr, R. G. *Phys. Rev. B* **1988**, *37*, 785.
- (44) Hehre, W. J.; Ditchfield, R.; Pople, J. A. *J. Chem. Phys.* **1972**, *56*, 2257.
- (45) Hay, P. J.; Wadt, W. R. *J. Chem. Phys.* **1985**, *82*, 299.
- (46) Peach, M. J. G.; Williamson, M. J.; Tozer, D. J. *J. Chem. Theory Comput.* **2011**, *7*, 3578.
- (47) Peach, M. J. G.; Tozer, D. J. *J. Phys. Chem. A* **2012**, *116*, 9783.
- (48) Yanai, T.; Tew, D. P.; Handy, N. C. *Chem. Phys. Lett.* **2004**, *393*, 51.
- (49) Tamm, I. *J. Phys. (USSR)* **1945**, *9*, 449.
- (50) Dancoff, S. M. *Phys. Rev.* **1950**, *78*, 382.
- (51) Hirata, S.; Head-Gordon, M. *Chem. Phys. Lett.* **1999**, *314*, 291.
- (52) Cosier, J.; Glazer, A. M. *J. Appl. Crystallogr.* **1986**, *19*, 105.
- (53) Dolomanov, O. V.; Bourhis, L. J.; Gildea, R. J.; Howard, J. A. K.; Puschmann, H. *J. Appl. Crystallogr.* **2009**, *42*, 339.
- (54) Lamansky, S.; Djurovich, P.; Murphy, D.; Abdel-Razzaq, F.; Kwong, R.; Tsyba, I.; Bortz, M.; Mui, B.; Bau, R.; Thompson, M. E. *Inorg. Chem.* **2001**, *40*, 1704.
- (55) Harvey, R. G.; Schmolka, S.; Cortez, C.; Lee, H. M. *Synth. Commun.* **1988**, *18*, 2207.
- (56) Ionkin, A. S.; Marshall, W. J. *Inorg. Chem.* **2005**, *44*, 6244.
- (57) Ionkin, A. S.; Marshall, W. J.; Wang, Y. *Organometallics* **2005**, *24*, 619.
- (58) Ionkin, A. S.; Marshall, W. J.; Roe, D. C.; Wang, Y. *Dalton Trans.* **2006**, 2468.
- (59) Hallett, A. J.; White, N.; Wu, W.; Cui, X.; Horton, P. N.; Coles, S. J.; Zhao, J.; Pope, S. J. A. *Chem. Commun.* **2012**, *48*, 10838.
- (60) Hay, P. J. *J. Phys. Chem. A* **2002**, *106*, 1634.
- (61) Edkins, R. M.; Wriglesworth, A.; Fucke, K.; Bettington, S. L.; Beeby, A. *Dalton Trans.* **2011**, *40*, 9672.
- (62) Passerini, R.; Ross, I. G. *J. Sci. Instrum.* **1953**, *30*, 274.
- (63) Ma, L.; Guo, H.; Li, Q.; Guo, S.; Zhao, J. *Dalton Trans.* **2012**, *41*, 10680.
- (64) Shavaleev, N. M.; Monti, F.; Costa, R. D.; Scopelliti, R.; Bolink, H. J.; Ortí, E.; Accorsi, G.; Armaroli, N.; Baranoff, E.; Grätzel, M.; Nazeeruddin, M. K. *Inorg. Chem.* **2012**, *51*, 2263.

- (65) Xu, M.; Wang, G.; Zhou, R.; An, Z.; Zhou, Q.; Li, W. *Inorg. Chim. Acta* **2007**, *360*, 3149.
- (66) Edkins, R. M.; Bettington, S. L.; Goeta, A. E.; Beeby, A. *Dalton Trans.* **2011**, *40*, 12765.
- (67) Pourtois, G.; Beljonne, D.; Moucheron, C.; Schumm, S.; Kirsch-De Mesmaeker, A.; Lazzaroni, R.; Brédas, J.-L. *J. Am. Chem. Soc.* **2003**, *126*, 683.
- (68) Kammer, S.; Starke, I.; Pietrucha, A.; Kelling, A.; Mickler, W.; Schilde, U.; Dosche, C.; Kleinpeter, E.; Holdt, H.-J. *Dalton Trans.* **2012**, *41*, 10219.
- (69) Velusamy, M.; Thomas, K. R. J.; Chen, C.-H.; Lin, J. T.; Wen, Y. S.; Hsieh, W.-T.; Lai, C.-H.; Chou, P.-T. *Dalton Trans.* **2007**, 3025.
- (70) Rillema, D. P.; Blanton, C. B.; Shaver, R. J.; Jackman, D. C.; Boldaji, M.; Bundy, S.; Worl, L. A.; Meyer, T. J. *Inorg. Chem.* **1992**, *31*, 1600.
- (71) Kapturkiewicz, A.; Nowacki, J.; Borowicz, P. *Electrochim. Acta* **2005**, *50*, 3395.
- (72) Brock, C. P.; Minton, R. P. *J. Am. Chem. Soc.* **1989**, *111*, 4586.
- (73) Parac, M.; Grimme, S. *Chem. Phys.* **2003**, *292*, 11.
- (74) Weber, L.; Eickhoff, D.; Marder, T. B.; Fox, M. A.; Low, P. J.; Dwyer, A. D.; Tozer, D. J.; Schwedler, S.; Brockhinke, A.; Stämmler, H. G.; Neumann, B. *Chem.—Eur. J.* **2012**, *18*, 1369.
- (75) Gu, X.; Fei, T.; Zhang, H.; Xu, H.; Yang, B.; Ma, Y.; Liu, X. *J. Phys. Chem. A* **2008**, *112*, 8387.
- (76) Peach, M. J. G.; Benfield, P.; Helgaker, T.; Tozer, D. J. *J. Chem. Phys.* **2008**, *128*, 044118.
- (77) Volpi, G.; Garino, C.; Nervi, C. *Dalton Trans.* **2012**, *41*, 7098.
- (78) Kowalczyk, T.; Yost, S. R.; Van Voorhis, T. *J. Chem. Phys.* **2011**, *134*, 054128.